



## Integrating airborne hyperspectral imagery and LiDAR for volcano mapping and monitoring through image classification

G. Kereszturi<sup>a,\*</sup>, L.N. Schaefer<sup>b</sup>, W.K. Schleiffarth<sup>c</sup>, J. Procter<sup>a</sup>, R.R. Pullanagari<sup>a</sup>, S. Mead<sup>a</sup>, Ben Kennedy<sup>b</sup>

<sup>a</sup> Geosciences, School of Agriculture and Environment, Massey University, Private Bag 11 222, Palmerston North, New Zealand

<sup>b</sup> Department of Geological Sciences, University of Canterbury, Private Bag 4800, Christchurch, New Zealand

<sup>c</sup> School of Earth Sciences and Environmental Sustainability, Northern Arizona University, Flagstaff, Arizona, USA



### ARTICLE INFO

#### Keywords:

Hydrothermal alteration  
Geological mapping  
Volcano  
Debris flow  
LiDAR  
Hyperspectral imaging  
Imaging spectroscopy  
Airborne remote sensing  
Image fusion

### ABSTRACT

Optical and laser remote sensing provide resources for monitoring volcanic activity and surface hydrothermal alteration. In particular, multispectral and hyperspectral imaging can be used for detecting lithologies and mineral alterations on the surface of actively degassing volcanoes. This paper proposes a novel workflow to integrate existing optical and laser remote sensing data for geological mapping after the 2012 Te Maari eruptions (Tongariro Volcanic Complex, New Zealand). The image classification is based on layer-stacking of image features (optical and textural) generated from high-resolution airborne hyperspectral imagery, Light Detection and Ranging data (LiDAR) derived terrain models, and aerial photography. The images were classified using a Random Forest algorithm where input images were added from multiple sensors. Maximum image classification accuracy (overall accuracy = 85%) was achieved by adding textural information (e.g. mean, homogeneity and entropy) to the hyperspectral and LiDAR data. This workflow returned a total surface alteration area of ~0.4 km<sup>2</sup> at Te Maari, which was confirmed by field work, lab-spectroscopy and backscatter electron imaging. Hydrothermal alteration on volcanoes forms precipitation crusts on the surface that can mislead image classification. Therefore, we also applied spectral matching algorithms to discriminate between fresh, crust altered, and completely altered volcanic rocks. This workflow confidently recognized areas with only surface alteration, establishing a new tool for mapping structurally controlled hydrothermal alteration, evolving debris flow and hydrothermal eruption hazards. We show that data fusion of remotely sensed data can be automated to map volcanoes and significantly benefit the understanding of volcanic processes and their hazards.

### 1. Introduction

The complexity of long-lived volcanic systems may be lost in remote sensing-derived geological maps that only consider topographic information. Hence, considering additional information (e.g. spectral data) in surface mapping can improve the recognition of landforms and surface processes unique to volcanic terrains (e.g. Kruse, 2012).

Imaging spectroscopy, or hyperspectral imaging, measures reflected, absorbed and emitted light of objects at many narrow and contiguous wavelengths in the Visible and Near-Infrared (VNIR; 350–1000 nm) and Shortwave Infrared regions (SWIR; 1000–2500 nm) (Goetz et al., 1985; Vane et al., 1993; Plaza et al., 2009). Space and airborne hyperspectral sensors, such as Airborne Visible/Infrared Imaging Spectrometer (AVIRIS), Reflective Optics System Imaging Spectrometer (ROSIS), Compact Airborne Spectrographic Imager (CASI),

Hyperion on the EO-1 satellite, HyMAP, Multispectral Infrared and Visible Imaging Spectrometer (MIVIS) and Specim AisaFENIX, are among the most commonly used hyperspectral sensors (Kunkel et al., 1991; Chen et al., 1999; Hellman and Ramsey, 2004; Forzieri et al., 2013; Hosseini Zadeh et al., 2014; Magendran and Sanjeevi, 2014; Swayze et al., 2014; Huesca et al., 2016; Pullanagari et al., 2016; Sun et al., 2016; Feng et al., 2018).

Geological mapping and mineral exploration can benefit from hyperspectral imaging due to indicator minerals with characteristic absorption features in the VNIR and SWIR regions of the electromagnetic spectrum (Clark, 1999; van der Meer, 2018; Carrino et al., 2018; Liu et al., 2018). In the VNIR region, the most detectable changes are due to the transfer of electrons between the atomic energy levels in elements such as iron ( $\text{Fe}^{2+}$  and  $\text{Fe}^{3+}$ ), manganese (Mn), nickel (Ni) and chromium (Cr). Thus, the VNIR region is particularly useful for detecting

\* Corresponding author.

E-mail address: [G.Kereszturi@massey.ac.nz](mailto:G.Kereszturi@massey.ac.nz) (G. Kereszturi).

minerals such as hematite ( $\text{Fe}_2\text{O}_3$ ), goethite ( $\text{FeO}(\text{OH})$ ) and jarosite ( $\text{KFe}_3^{3+}(\text{OH})_6(\text{SO}_4)_2$ ) (Kruse et al., 1993; Clark, 1999; Murphy and Monteiro, 2013; Magendran and Sanjeevi, 2014; van der Meer, 2018; De Boissieu et al., 2018). The SWIR region provides a proxy for detecting vibrational features of Al–OH, Mg–OH, C–O-bearing minerals such as sulphates, carbonates, micas, and clay minerals. The presence of the latter is an indicator of hydrothermal alteration, or change in mineralogy as a result of hot water interacting with the rocks, and ore mineralization (Kruse et al., 1993; Crowley et al., 2003b; Kruse et al., 2012; Swayze et al., 2014). The use of hyperspectral remote sensing for surface geological mapping and mineral alteration detection has been employed mostly in exploration geology using Hyperion, HyMAP and AVIRIS data (e.g. Bedini et al., 2009; Magendran and Sanjeevi, 2014), and spectral matched linear filtering methods (Kruse et al., 1993; Boardman et al., 1995; Rogge et al., 2014).

For volcano and geothermal research, Landsat series and Advanced Spaceborne Thermal Emission and Reflection Radiometer (ASTER) have been used extensively (Pieri and Abrams, 2004; Vaughan et al., 2005; Mia and Fujimitsu, 2012; Tayebi et al., 2014; van der Meer et al., 2014). Moreover, a great variety of research has been published using Light Detection and Ranging (LiDAR) technology to explore volcanic terrains and volcano-related hazards (Spinetti et al., 2009; Keresztsuri et al., 2012; Tarquini et al., 2012; Whelley et al., 2014; Behncke et al., 2016). In contrast, hyperspectral imagery has rarely been employed for volcano geological mapping. These include mineral alteration mapping using spectral matched linear filtering methods (e.g. Boardman et al., 1995), such as at the Mauna Kea volcano in Hawaii (Guinness et al., 2007), and Mt. Shasta and Mt. Rainier volcanoes in the western USA (Crowley and Zimbelman, 1997; Crowley et al., 2003a). Other studies have used hyperspectral imagery to estimate  $\text{CO}_2$  concentrations in volcanic plumes at Kilauea in Hawaii (Spinetti et al., 2008), map thermal structure of an active lava flow on Mt Etna in Italy (Lombardo et al., 2009), and create geological maps of Hekla volcano in Iceland (Waske et al., 2009). Spectral information combined with the recent developments in statistical learning for image classification and regression (e.g. Mountrakis et al., 2011; Cracknell and Reading, 2014; Pullanagari et al., 2016; Toniol et al., 2017) can provide insights for geological applications with importance to understanding complex volcanic systems, volcanic hazards, and geothermal resources.

This paper combines airborne hyperspectral data, high-resolution optical imagery, and Light Detection and Ranging (LiDAR) topographic data to map and identify volcanic deposits based on spectral and textural signatures. The developed workflow uses pixel-wise image stacking and image classification to provide an updated surface geological map after the 2012 eruptions of the Te Maari craters, Tongariro Volcanic Complex, New Zealand (Fig. 1A and B). In 2012, Te Maari craters produced two phreatic eruptions, one of which was landslide-triggered highlighting the need to study hydrothermal alteration on volcanoes using a combination of field, analytical and remote sensing techniques. Hence, the present study aims to provide a surface mapping workflow that can be integrated into volcanic hazard assessments (e.g. hydrothermal alteration mapping, delimitation of potential debris flow source zones) and efforts to understand volcanic processes (e.g. identification of sediment transport processes).

## 2. Study area, materials and data processing

### 2.1. Geological setting

The Tongariro Volcanic Centre is located in the southern extremity of the Taupo Volcanic Zone, formed in a back-arc setting due to an oblique westward subduction of the Pacific Plate beneath the Australian Plate (Houghton et al., 1995; Wilson et al., 1995). The volcanic zone is dominated by NE-SW-oriented normal faulting of the Taupo rift system that is dominated by extension and high heat flux (Bibby et al., 1995; Villamor and Berryman, 2006; Gómez-Vasconcelos et al., 2016). The

basement around the Tongariro volcanic complex is made of the Mesozoic Torlesse Terrain and Waipapa Terrane units that is mostly comprised of greywacke (Townsend et al., 2017). These units are overlain by Cenozoic marine sedimentary rocks and Quaternary lava and volcaniclastic rocks (Townsend et al., 2017).

Volcanism at the Tongariro Volcanic Centre has developed an elongated NE-SW vent zone roughly 14 km long by 5 km wide. This vent zone has at least 15 highly overlapped individual cones each with a volume of  $> 0.5 \text{ km}^3$  that show no spatial and temporal trend over the last 275 ky (Hobden et al., 1996; Nairn et al., 1998; Hobden et al., 1999). Volcanic activity at the Tongariro Volcanic Centre is characterised by frequent, small-volume eruptions ( $0.1\text{-}1 \text{ km}^3$ ), forming a highly coalescent and dissected volcanic complex. The erupted magmas have intermediate compositions spanning from basaltic-andesite to dacite (Nakagawa et al., 1998; Hobden et al., 2002; Shane et al., 2017). Most eruptions in the post-glacial era have erupted from multiple vents located around the Te Maari craters and Red Crater (Scott and Potter, 2014; Miller and Williams-Jones, 2016).

The most recent eruptions occurred at the upper Te Maari crater on the 6<sup>th</sup> August and 21<sup>st</sup> November 2012 (Fig. 1A and B). These short-lived eruptions (< 1 min) deposited a thin veneer of ash over an area of  $1600 \text{ km}^2$  (Pardo et al., 2014; Turner et al., 2014). The August eruption was triggered due to decompression of the hydrothermal system after a seismically-induced landslide uncapped ca.  $7 \times 10^6 \text{ m}^3$  of material from the northern flanks (Jolly et al., 2014; Pardo et al., 2014; Procter et al., 2014). The landslide evolved into a debris flow that traveled for 2 km, covering the upper catchment of the Mangatipua stream with a mixture of hydrothermally altered breccia, agglutinated scoria and spatter deposits in a clay-rich matrix (Fig. 1B). The host rock of the landslide was a moderate to highly altered agglutinated and welded to non-welded scorriaceous deposits from the Blue Lake Crater. These welded scorriaceous deposits forms from mechanical compaction of the fluidal particles after deposition, while agglutination is a heat-driven sticking of particles together (e.g. Sumner et al., 2005). The eruption produced multiple lateral blasts and an eruption column as high as 10 km (Pardo et al., 2014; Turner et al., 2014; Montanaro et al., 2016). Evidence suggests that the landslide slip surface occurred through a highly altered scorriaceous pyroclastic deposit (Procter et al., 2014). This hazard scenario had not been foreseen based on the preserved geological record. However, areas of pervasive hydrothermal alteration are known to exist in the Tongariro Volcanic Complex that are generally produced due to circulation of hydrothermal fluids through the various edifices (Brock and Brock, 1971; Miller and Williams-Jones, 2016; Miller et al., 2018). One prominent area is the Ketetahi Springs, which has numerous fumaroles, mud pools and hot springs that precipitate iron hydroxides and sulphur (Brock and Brock, 1971; Moore and Brock, 1981). The ongoing alteration around the Ketetahi and Te Maari areas weakens volcanic rocks and deposits, posing potential hazards to both population (e.g. hikers along the frequently visited Tongariro Alpine Crossing Track) and critical infrastructure (e.g. State Highway 46).

### 2.2. Instrumentation, aerial-surveys and image processing

The airborne hyperspectral survey was carried out at Tongariro Volcanic Centre between 12:25 and 13:43 local time on the 7 April 2016 (UTC + 12 h) with a push-broom, full-spectrum AisaFENIX hyperspectral sensor (370–2500 nm). The spectral sampling interval was between 3.3 and 5.7 nm from VNIR and SWIR region with a full-width-at-half-maximum of 3.2–12.2 nm. The AisaFENIX has a total Field of View of 32.2°, and an Instantaneous Field of View of 0.084°. The misalignment between the Oxford Survey + GPS/IMU unit and the AisaFENIX sensor was reduced by applying boresight corrections to the imagery, based on a calibration flight. The GPS/IMU data was post-processed to reach an accuracy under a pixel (< 2 m) using permanent ground GPS station data from stations closer than 50 km from a survey site. The swaths were orientated from N (170°–190°) and S (350°–10°)

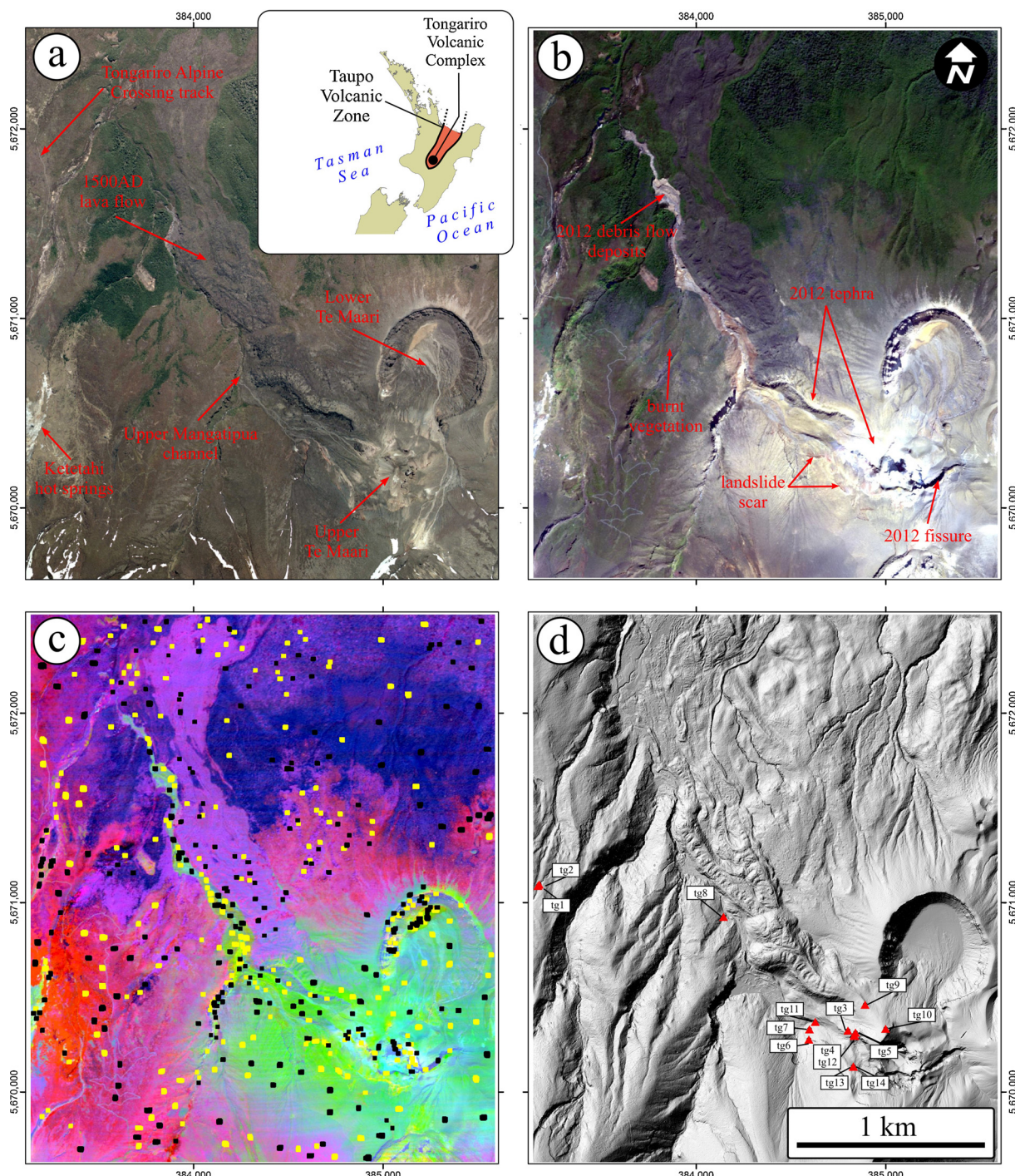


**Fig. 1.** (a) Pre-2012 orthophoto of the Te Maari area on Tongariro Volcanic Complex. The inset map shows the location of the Tongariro Volcanic Complex within the North Island of New Zealand. (b) True colour composite of the high-resolution hyperspectral image with the major topographic and volcanic features of the Upper Te Maari area. (c) The distribution of the training (yellow) and validation pixel (black) overlaid on the MNF reduced hyperspectral data. The first three bands are shown as RGB. (d) Hillshade image derived from the LiDAR dataset of the Te Maari area showing the sampling locations.

to minimize the Bidirectional Reflectance Distribution Function (BRDF) effects. Each strip was surveyed at solar elevations  $\geq 40^\circ$ , in cloud-free conditions, and at aircraft speeds of 105–115 knots to maximize exposure time of the ground objects. Flight height was about 1300 m above ground level, resulting in a ground resolution of 2 m. During aerial surveying, a spectral binning setting of  $4 \times 2$  was used in the VNIR to enhance signal strength, resulting in 448 spectral bands. No spectral binning was used in the SWIR region. The hyperspectral flight settings and imaging geometry are summarized in Table 1.

The AisaFENIX sensor has a small fraction of malfunctioning

detectors ( $\leq 1\%$  in the SWIR region), resulting in vertical lines with constant Digital Number (DN) values. Vertical striping in the raw imagery is common due to the push-broom imaging technology, such as for AisaFENIX (Pullanagari et al., 2016) and Hyperion (Kruse et al., 1993). The faulty values in the imagery were located using a sensor-specific map of bad detectors and replaced using neighboring spectral band data. The bad detector corrected imagery with DN was then converted to radiance ( $\text{W}/\text{m}^2/\text{sr}$ ) in CaliGeoPRO (Fig. 2). The georectification was carried out using a smoothed, contour-based Digital Elevation Model from linear interpolation. The imagery was then

**Table 1**  
Hyperspectral survey and atmospheric correction settings used in this study.

Parameter	Unit	Hyperspectral survey	
spatial resolution	m	2	
spectra sampling interval	nm	3.4 (VNIR)	5.6 (SWIR)
full width at half maximum	nm	3.0 (VNIR)	10.9 (SWIR)
spectral binning	–	VNIR	4 × 2
	–	SWIR	1 × 1
data acquisition frame rate	fps	62	
exposure time	ms	VNIR	15.1
	ms	SWIR	13.9
flight height	m agl	1350	
aircraft speed	km/h	194–213	
number of strips	nr	15	
solar azimuth	deg.	332.5–357.8	
solar elevation	deg.	40.1–43.9	
solar zenith	deg.	46.1–49.9	
water vapour column	g/cm	1.0	
water vapour retrieval band	nm	1130 nm	
visibility	km	50	
aerosol model	–	rural	

further compensated for atmospheric effects using a MODTRAN5 model implemented in the ATCOR-4 software (Richter and Schlüfer, 2002). The parameters used for atmospheric correction are shown in Table 1. The strips were processed separately and mosaicked seamlessly together before spatial subsetting to match the LiDAR data extent (Fig. 2).

The airborne LiDAR and photography survey was carried out on 8–9 November 2012 using an Optech ALTM 3100 EA LiDAR system and Trimble Aerial Camera, respectively. Both systems were used along with GPS/IMU and processed with Applanix POSPac software. The flying height of the plane was set to 1200 m above the lowest ground (northern corner of the ground cover). The instrument was operated with a scan angle of 38°, a laser pulse rate of 70 kHz and mirror scan frequency of 41.2 Hz. The overlap between swaths was 50%. The point cloud on the ground had 3 returns/m<sup>2</sup>. The raw point cloud was then converted into a Triangular Irregular Network (TIN) model before gridding to a Digital Terrain Model (Fig. 2). Both LiDAR and optical imagery were captured in New Zealand Transverse Mercator Projection, and later re-projected and co-registered with an RMSE error of 1.6 m (< 1 pixel on the ground) and 0.8 m (< 1.6 pixels on the ground) with the hyperspectral image cube, respectively (Fig. 2).

### 2.3. Field sampling, spectroscopy and energy dispersive X-ray spectroscopy

Field campaigns for sampling and ground validation were carried out in early 2017, which investigated hydrothermally altered deposits and products of the last 2012 eruptions (Figs. 1D and 3). A total of 14 lithologies of various compositions and textures were sampled in the field (Fig. 1D), which were subsequently analysed using laboratory-based spectroscopy and Scanning Electron Microscope (SEM). The samples were analysed by a FieldSpec 4 Hi-Res spectroradiometer in laboratory conditions using a contact probe with a sampling footprint of

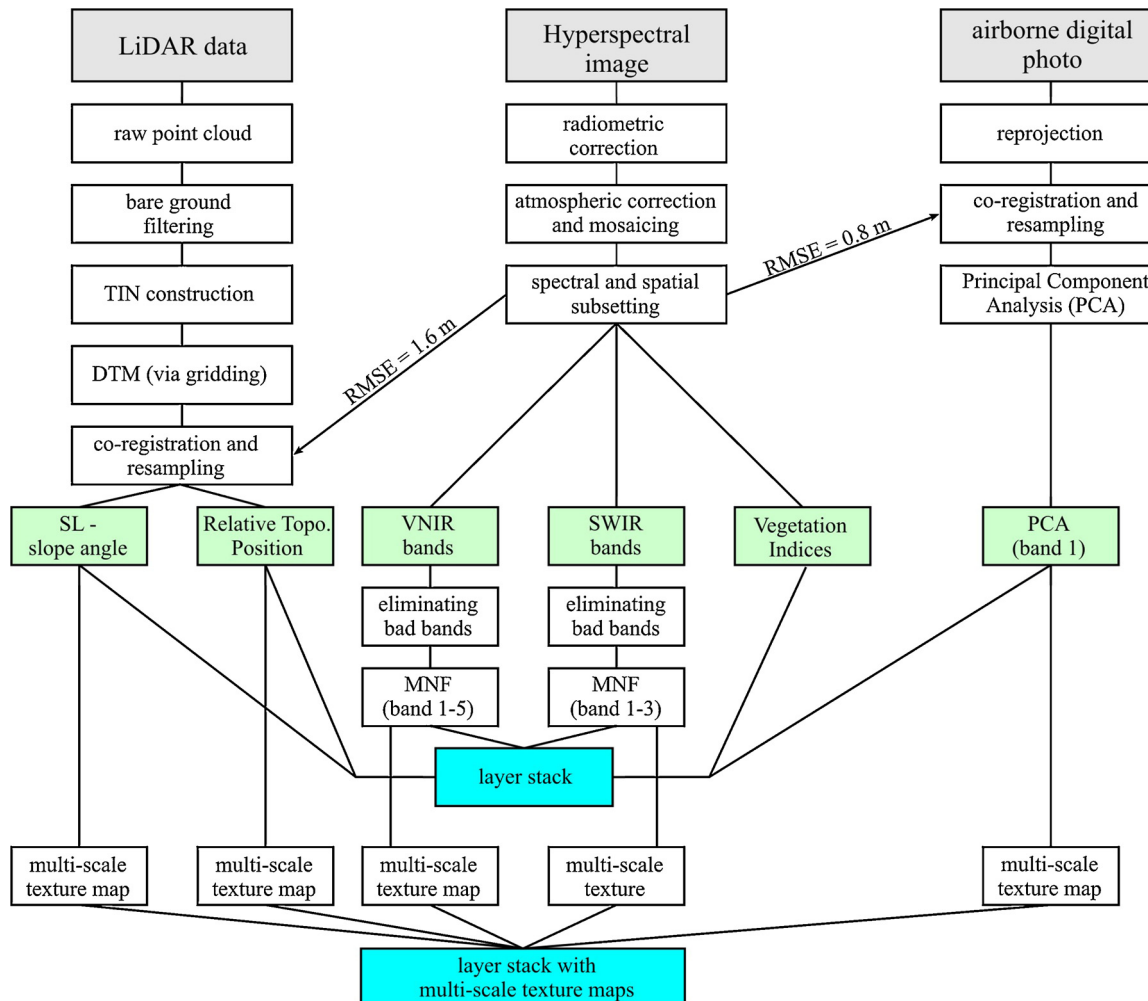


**Fig. 2.** Work flow of multi-sensor data fusion using LiDAR, airborne hyperspectral and airborne photography. For detailed explanation, the reader is referred to the text.

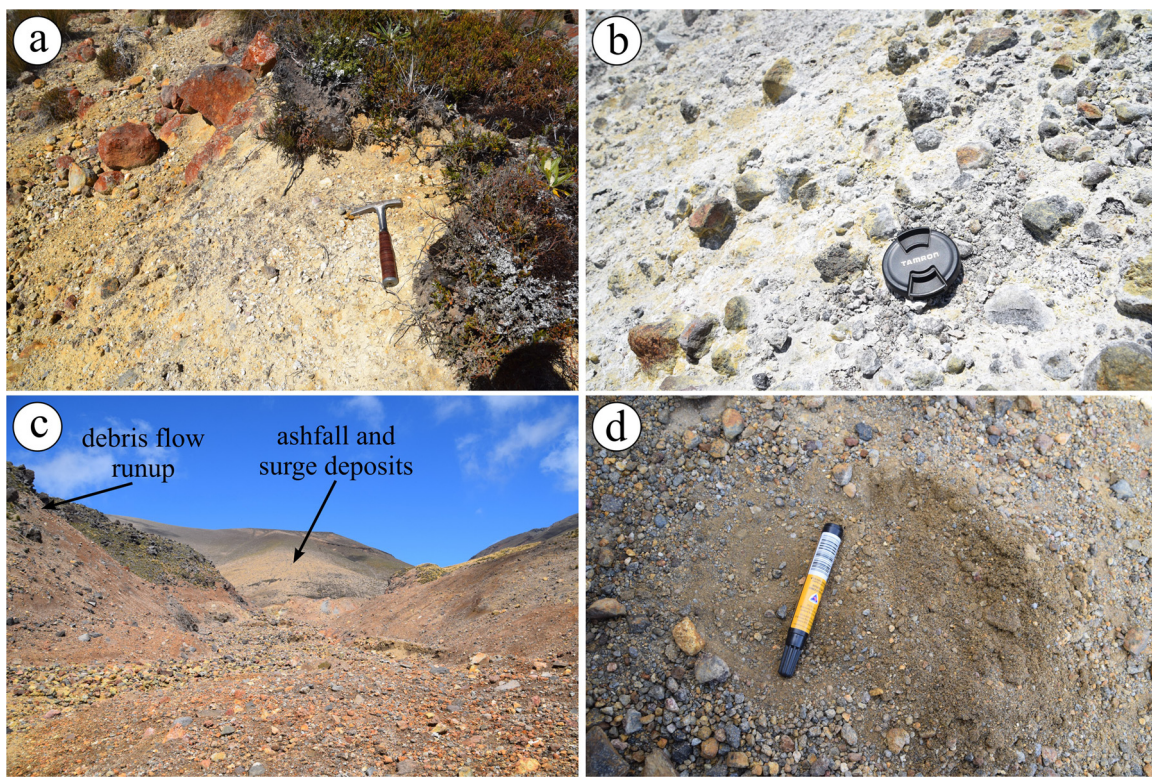


**Fig. 3.** Field photos of the sample sites around the Te Maari area. (A) Hydrothermally altered and reworked deposits along the outlet valley from Ketetahi springs, (B) Hydrothermally altered deposits with blocks fragment and patches of sulphur precipitation located close to the Upper Te Maari crater, (C) Upper-catchment of the Mangatipua stream with the debris flow deposits. The poorly sorted deposits are made of mostly hydrothermally altered angular to sub-angular blocks. (D) Close-up photo of the ash-fall and surge deposits from the 2012 Te Maari eruption about 300 m from its source.

**Table 2**

Input data definition. Inputs with asterisk have been used to derive multi-scale textural using grey-scale co-occurrence matrices.

Input data group	Data source	Layer	Definition/reference
SWIR	Hyperspectral imaging	band 1*	MNF reduced band from the SWIR sensor
		band 2*	MNF reduced band from the SWIR sensor
		band 3*	MNF reduced band from the SWIR sensor
VNIR	Hyperspectral imaging	band 1*	MNF reduced band from the VNIR sensor
		band 2*	MNF reduced band from the VNIR sensor
		band 3*	MNF reduced band from the VNIR sensor
		band 4*	MNF reduced band from the VNIR sensor
		band 5*	MNF reduced band from the VNIR sensor
VEG	Hyperspectral imaging	NDVI	$\frac{(b800 - b650)}{(b800 + b650)}$
		SR	$\frac{b800}{b650}$
		EVI	$2.5 * \frac{(b800 - b650)}{(b800 + 6b650 - 7.5b480 + 1)}$
		MRESR	$\frac{(b750 - b445)}{(b705 + b445)}$
		MRENVI	$\frac{(b750 - b705)}{(b750 + b705 - 2b445)}$
PHO LiDAR	Aerial photograph Digital Terrain Model	band 1*	PCA reduced single band image from 2012 aerial photos
		SL - slope*	Average, linear filter slope angle of the LiDAR DTM
		RTP* - Relative Topographic Position	$\frac{Z_i}{Z_{all}}$

These were calculated for the mean ( $\bar{m}$ ), homogeneity ( $\bar{h}$ ) and entropy ( $\bar{e}$ ) as:

$$\bar{m} = \sum_{i=1}^N \sum_{j=1}^N ij * P(i, j)$$

$$\bar{h} = \sum_{i=1}^N \sum_{j=1}^N \frac{1}{1 + (i - \bar{m})^2} * P(i, j)$$

$$\bar{e} = \sum_{i=1}^N \sum_{j=1}^N P(i, j)^2 \log P(i, j)$$

where N is the number of grey-scale (i.e. 255), i and j are the location of pixel pair within the moving window, P is the probability of the value to occur within a pixel pair at 1 pixel shifts in direction of 0°, 45°, 90° and 135°. For the vegetation indices the parameters b represent band, while the subscript represent the wavelength. In the RTP, Z is the elevation of the central cell i, while  $Z_{all}$  is the mean cell elevation on a moving window (i.e. 3 × 3, 11 × 11, and 21 × 21).

**Table 3**

Training and validation datasets using in this study.

Classes	Training data nr. of pixels	Test data nr. of pixels
1 - vegetation (forest, scrub)	621	598
2 - dead vegetation	318	329
3 - shadow	345	351
4 - Rotopunga scoria (non-welded)	100	23
5 - Rotopunga scoria (welded)	156	139
6 - North Crater scoria (non-welded)	234	225
7 - lava flow 1 (North Crater)	511	527
8 - lava flow 2 (North Crater)	330	325
9 - 1500 AD lava flow (Te Maari)	91	104
10 - 2012 debris flow (Te Maari)	384	335
11 - 2012 tephra (Te Maari)	753	743
12 - hydrothermal alteration (Te Maari)	160	166
13 - reworked deposit (Te Maari)	175	177
14 - alluvial deposit (Blue & Sulphur Lakes)	115	118
15 - alluvial deposit (Ketetahi springs)	103	99
Total	4396	4259

10 mm in diameter. To ensure the samples were consistently dry for spectral measurements, samples were placed in an oven for 12 h before analysis at 40 °C. Before scanning the samples, the instrument readings were calibrated using a white Spectralon Diffuse Reflectance Standard. In total, 100 spectral measurements were recorded that were averaged using View Spec Pro software. In total, 3–6 spot measurements of each sample were taken to represent the reflectance signatures of the sampled alteration units. Once the reflectance values were measured in the laboratory they were used to provide ground reference data and high

accuracy spectral data for mineral identification. Minerals were identified by matching the spectral curves to the USGS Spectral Library (Clark et al., 2007) using Spectral Angle Mapper (SAM) and Spectral Fitting Function (SFF) in ENVI software.

Thin section were prepared from block samples, cut to preserve the exterior (crust) and interior of the samples, and polished in preparation for Scanning Electron Microscopy (SEM) analysis. A representative area of each slide was chosen to produce a Back Scattered Electron (BSE) image and spot detection of element abundances using Energy-dispersive X-ray Spectroscopy (EDS). EDS analyses examined the extent of alteration by identifying alteration minerals and any changes in composition and texture from the crust to the interior of each sample.

#### 2.4. Geological mapping using multiple image inputs

Spectral information can distinguish minerals (e.g. van der Meer et al., 2018), while topographic information from LiDAR data can be used to discriminate lithological units based on topographic position and surface textures (e.g. Whelley et al., 2014). Hence, the motivation of this study is to combine data from several sensors to improve the image classification accuracy for volcano surface mapping. This is especially useful for highlighting areas with increased hydrothermal alteration that are potential hazards sources (e.g. debris flows, landslides and hydrothermal eruptions).

The input data for the image classification is summarized in Fig. 2 and Table 2. The hyperspectral image was spectrally resampled by eliminating noisy bands (e.g. < 400 nm, > 2400 nm, and between 1950–2000 nm), which reduced the effective bands from 448 to 388

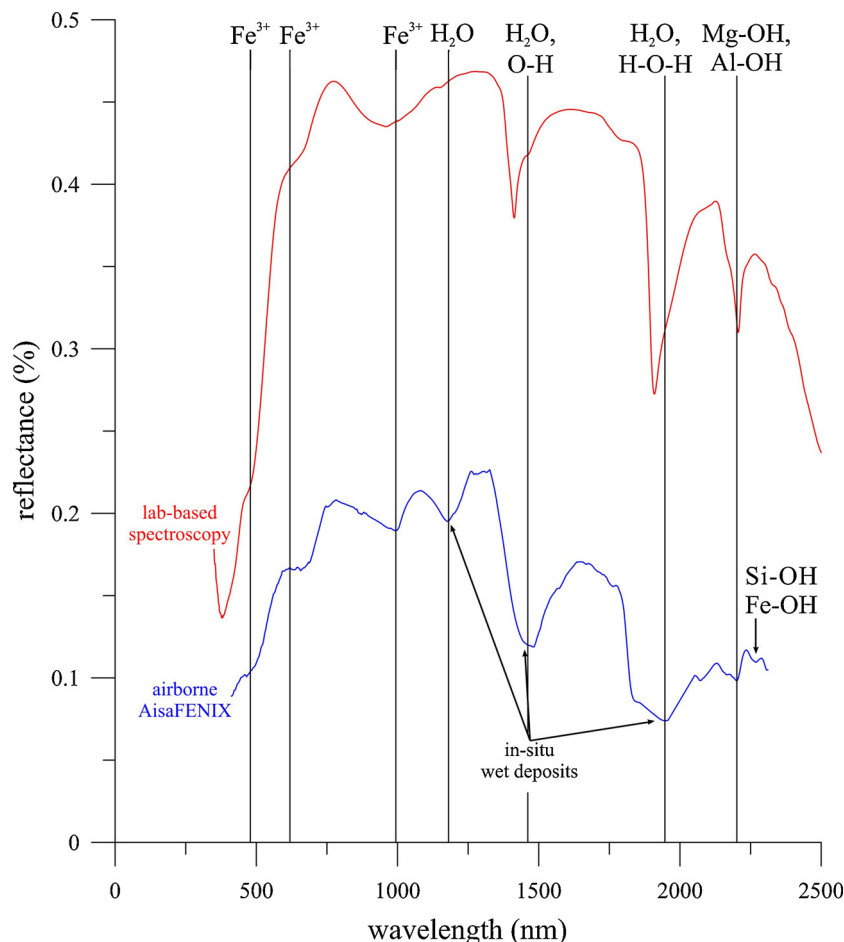


**Fig. 4.** Composition of the spectra collected by laboratory-based spectrometer (red curve) and by airborne imaging (blue curve) after corrections over hydrothermally altered alluvium (sample: tg03). The vertical line are the major absorption features related to electron transition and OH features.

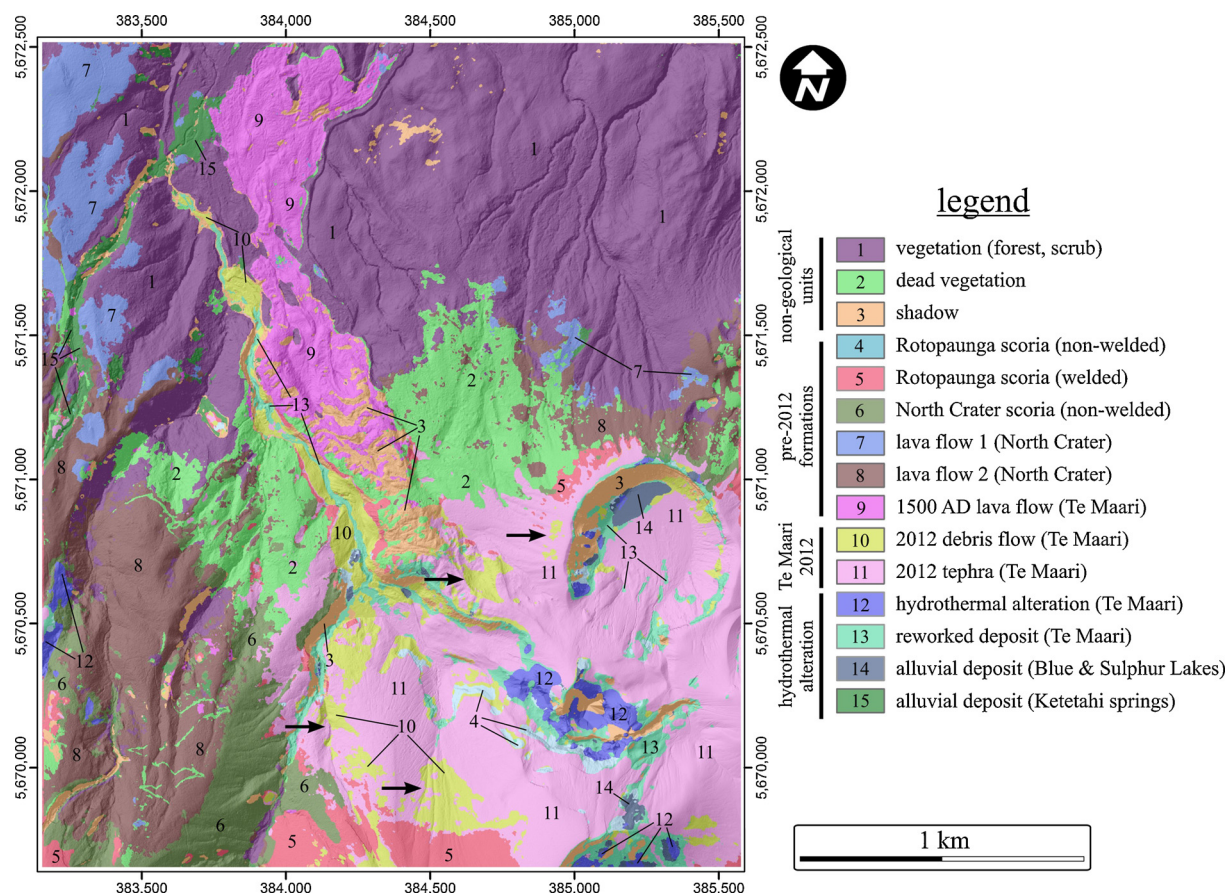


**Fig. 5.** Geological map obtained from image classification with the OA = 85%. The classified image is overlaid on top of the hillshade image from LiDAR to emphasize the topographic variability across the scene. The horizontal arrows highlights some misclassification of Class 10 and 11 (debris flow and tephra deposits from the 2012 Te Maari eruption) due to the spectrally similar compnentry of the lithologies.

(Fig. 2). Moreover, the VNIR (380–970 nm) and SWIR (970–2500 nm) image data was processed separately due to contrasting levels of noise and different detector types (e.g. Complementary Metal-Oxide-Semiconductor for VNIR, and Mercury-Cadmium-Telluride for SWIR). This study used Minimum Noise Fraction (MNF) to reduce the number of bands before image classification (Green et al., 1988). This applies a linear transformation, similar to the Principal Component Analysis, to rank the spectral data based on noise levels (Green et al., 1988). This study used the first 5 and 3 MNF bands for VNIR and SWIR respectively (Fig. 2), selected using the Eigenvalue plot ( $> 1$ ) and textural interpretation of the MNF bands (e.g. appearance of vertical lines due to the push-broom imaging system). This data was used to collect training and test populations for the supervised image classification. Besides these RGB colour composites of the MNF bands, the training and test data was also collated from field observations, hand-held GPS point data and previously published geological maps of the area (e.g. Townsend et al., 2017).

To improve the generalization of the output maps, textural maps of the input images were calculated using grey-level co-occurrence matrix (e.g. Haralick et al., 1973) on moving window sizes of  $3 \times 3$ ,  $11 \times 11$  and  $21 \times 21$  pixels (e.g. mean, homogeneity and entropy; Table 2). These input window sizes can discriminate landscape features at multi scales. For example,  $3 \times 3$  moving windows can pick up land surface elements the size of boulders (e.g. debris flow deposits), while the  $11 \times 11$  and  $21 \times 21$  moving window sizes target large geomorphic features, such as channels, ridges, and volcanic craters. Textural maps were integrated on a pixel-by-pixel basis using layer stacking. The input were summarized in Table 2. Each input groups were combined together step-by-step in the image classification to evaluate the

contribution of each data sources.

A Random Forest algorithm (Breiman, 2001) was chosen for image classification, which is found to be well-suited for geological application (Cracknell and Reading, 2014) due to its fast parameterization time and resistance to data co-linearity (e.g. Belgiu and Drăguț, 2016). This procedure includes the calculation of many simple decision tree models that provides a classification, which is combined with bootstrap aggregating procedure to recognize independent predictors (see recent review by Belgiu and Drăguț, 2016 and references therein). In this study, the total number of tree models was 500, which can provide enough generalization of the model (e.g. Belgiu and Drăguț, 2016). At each split, the square-root of input features was used as a model parameter. The random forest classifier was trained on a population subset (50%), and then validated using an independently collected test population (50%; Fig. 1C). In total, 15 classes have been identified based on the MNF bands, local geological information and field observations (Table 3). The accuracy of the classification was assessed using overall accuracy (OA), along with matrix of user's and producer's accuracies (defined as Liu et al., 2007). Kappa Accuracy was not considered in this study (c.f. Pontius and Millones, 2011). It is worth noting that OA measures were used in this study to quantify relative differences in the image classification accuracy between each input group.

### 3. Results and interpretations

#### 3.1. Surface mapping

Airborne hyperspectral data shows a good match to ground control data (e.g. match of absorption locations) for lava rocks, reworked

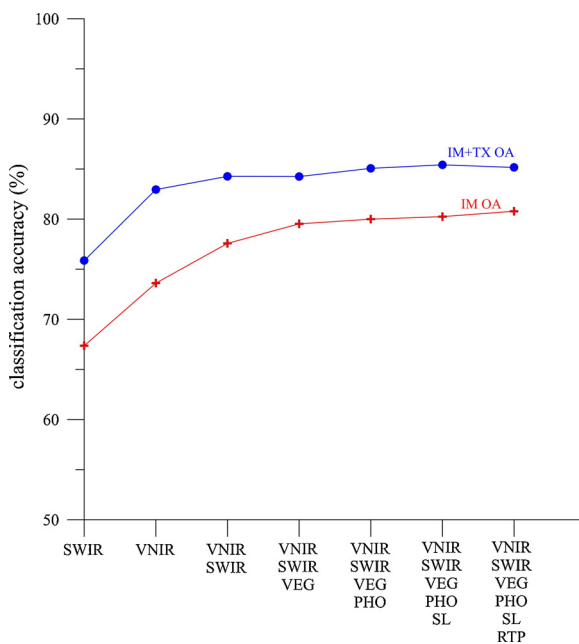


**Fig. 6.** Overall accuracy (OA) as a function of changing input imagery. IM (red crosses) is for only imagery, while IM + TX (blue circles) is imagery with multi-scale texture maps. The input image groups are: SWIR – The first three bands of the MNF-reduced SWIR sensor bands; VNIR - The first five bands of the MNF-reduced VNIR sensor bands; VNIR + SWIR – VNIR and SWIR combined; VEG –Vegetation Indices; PHO – Principal Component Analysis reduced high-resolution imagery from 2012; SL – Slope angle map derived from 2012 LiDAR DTM; RTP – Relative Topographic Position derived from 2012 LiDAR DTM.

volcanic tephra, and hydrothermally altered alluvium (Fig. 4). The airborne hyperspectral image captures the major absorption features of some mineral phases of interest in this study (e.g. hydroxyl-bearing minerals, Fig. 4). However, there is also a distinct contrast between the laboratory- and airborne survey derived spectra (Fig. 4) caused by the wetness of the in-situ deposits. This makes the water-related absorption features broader, preventing the recognition of the symmetry of mineral spectra at 1400 nm and 1900 nm regions (Fig. 4).

The main results from the classification are presented in Figs. 5 and 6. The image classification results represent a “hybrid” geological map that has some non-geological land surface cover types included (e.g. vegetation, dead vegetation due to volcanic activity). The rest of the map was divided into three groups: pre-2012 formation, Te Maari 2012 deposits, and hydrothermally altered deposits (Fig. 5). The unvegetated areas around the Te Maari crater provide useful insight into the stratigraphic (e.g. time sequences of lava flows from the Northern Cone and Te Maari) and sedimentological distinction of the lithologies (e.g. agglutination and welding and non-welding). This was picked by the image classification due to the spectral information from the hyperspectral image.

The input data stored as a layer stack made it possible to assess the contribution of each input group's contribution to the overall classification accuracy. The OA accuracies are plotted in Fig. 6. Only moderate classification accuracies were achieved (OA = 67–73%), considering only MNF bands from the hyperspectral image (e.g. VNIR and SWIR spectral regions). The image classification accuracy is increased by adding extra information from LiDAR and high-resolution airborne photos; however, the accuracy level plateaued at a relatively high accuracy of OA = 85% when all input images are combined (red line in Fig. 5). The user's and producer's accuracy are reported in Fig. 7.

The biggest improvement in accuracy is reached when textural elements were included, resulting in a +10% accuracy improvement (blue and red lines in Fig. 6). This improvement is due to the reduction of locally misclassified pixels and better model generalization

capability. The textural input images allowed the model to account for slight differences between subtle lithologies (e.g. distinction between agglutinated/welded and non-welded scoria, older lava flows, or in situ and reworked hydrothermal altered deposits), as shown in the user's and producer's accuracy figures (Fig. 8 and Table 4). Thus, this allowed for the identification of subtle depositional and genetic differences in an otherwise unvarying volcanic environment.

The error matrix highlights classes with spectral, topographic, and textural similarity among classes (e.g. dead scrub and older lava flow sequences, or the 2012 Te Maari tephra, surge deposits and debris flow deposits; Table 5). Spectrally, the 2012 Te Maari debris flow and tephra deposits look alike (e.g. Fig. 3C and D), posing difficulties in image classification. This has been overcome to some extent by including textural data (e.g. mean, homogeneity, entropy) and data from multiple sensors (e.g. topographic from LiDAR). The debris flow deposits are matrix-rich and poorly sorted with abundant blocks/boulders, while the tephra fall deposits are much finer grained (e.g. ash to lapilli grain size) and are moderately to well sorted (e.g. Fig. 3C and D). The topographic information from LiDAR feeds information into the classification process regarding the topographic position and potentially the deposit's depositional setting. For example, the debris flow emplacement was mostly confined by the Mangatipua channel (Figs. 1B and 5), while the tephra-fall deposits followed no topographic constraints. Similar improvement has been identified for the agglutinated/welded and non-welded scoria deposits, despite having spectral and geochemical similarity (e.g. North Cone and Rotopaunga scoria deposits). The user's and producer's accuracy improved significantly (e.g. from 5 to 55% to 90–100%) due to the input of topographic and textural data from LiDAR (Figs. 7 and 8). This means that the proposed classification workflow was able to pick up the signatures of agglutinated, welded and non-welded scoriaceous deposits. Distinction of welding and agglutination is important since these depositional processes govern rock straight, compaction and rock density. The textural maps of the VNIR bands improved mostly of distinction of the welded and agglutinated processes (e.g. Class 5 in Figs. 7 and 8). This is interpreted to be due to in situ oxidation due to heat, changing the VNIR spectra at around 500 nm and 880 nm (Hamilton et al., 2008; Keresztsuri and Németh, 2016).

Based on the field samples, linear spectral matching was also applied to the hyperspectral imagery using the Mixture Tuned Matched Filtering algorithm (Fig. 9). The end-members were sampled in the field, ranging from fresh (tg12 in Fig. 1D), to crust-altered with no interior alteration (tg13 in Fig. 1D), to pervasively altered lithologies (tg14 in Fig. 1D). The locations of those samples were used as end-members in the spectral matching procedure. The spectral matching produced a map of each end-member (Fig. 9A-D) that shows the match of airborne hyperspectral spectra with the selected alteration end-members. The spatial distribution of fresh and crust-altered hard rocks shows a good agreement that is promising in terms of predicting their subsurface properties. Pervasively altered rocks are mapped over a wider area around Te Maari (e.g. Fig. 9C) than observed in the field. This is due to the landslide/debris flow and tephra blasting associated with the 2012 eruptions that distributed considerable amounts of pervasively altered deposits as lithics, which are now exposed along the post-eruption landslide scarps (Fig. 1B and C).

### 3.2. Surface mineralogy and type of alteration

Hydrothermal alteration due to fluid-mineral interactions induces complex physio-chemical changes to volcanic rocks, which is controlled mostly by temperature, water-to-rock ratio, primary mineralogy of the host-rock, and fluid pH and chemistry (e.g. Miyoshi et al., 2013; Julia et al., 2014). The laboratory-based spectroscopy results (Table 6) show that the samples contain absorption features at 1420 nm, 1920 nm, and broader features at 2205 nm, consistent with hydroxyl-bearing clay minerals. The spectral matching algorithm, such as SAM and SFF, shows

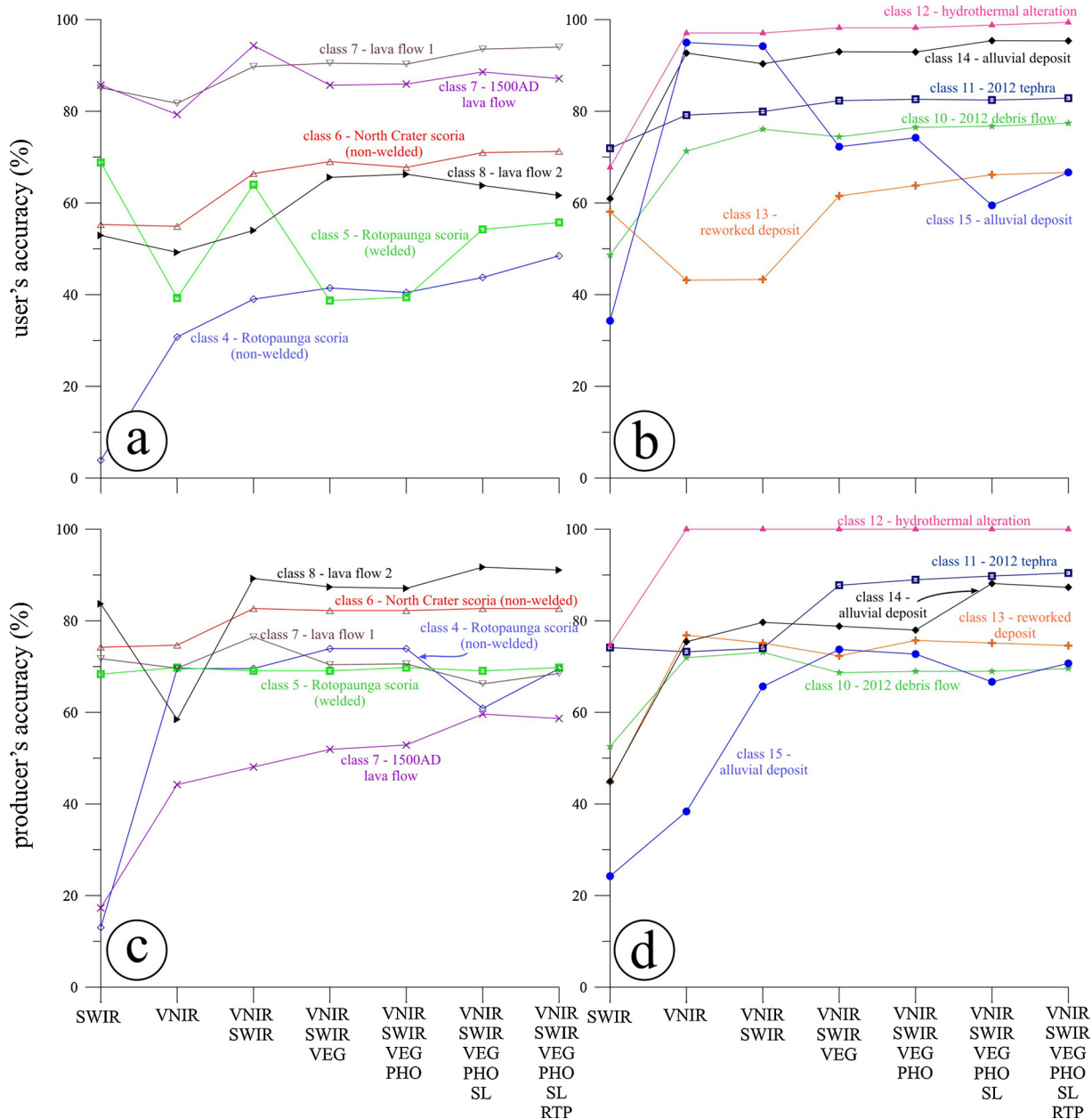


**Fig. 7.** User's and producer's accuracy measures as a function of different combination of image inputs.

that the most likely mineral phases in the collected sample belong to the phyllo- and tectosilicates, oxides, and sulphates (Table 6). The spectral signature of the field sample matches closely with spectral library curves of halloysite, kaolinite, rectorite, clinoptilolite, mordenite, illite and montmorillonite, nontronite, endellite, and hectorite (Table 6), which are weathering products of primary plagioclase with minor contribution from pyroxenes and amphibole phenocrysts and micro-crystals in the ground mass (Fig. 10). The samples also have a variety of spectral absorption features located in the VNIR region, notable around 380 nm and 680 nm, which are consistent with minerals such as goethite, hematite and sulphur. These mineral associations are typical of argillic to advanced argillic alteration of the primary volcanic rocks (e.g. van der Meer et al., 2012). This advanced argillic alteration can occur in atmospheric conditions, but at Te Maari it is due to the low-temperature ( $\leq 80$  °C) circulation of hydrothermal fluids and infiltration of surface water through porous and fractured volcanic deposits. This is consistent with water temperatures of 90 °C measured at the Ketetahi Springs with acidic to alkaline pHs, covering a wide range of

pH values between 3.0 and 8.0 (Brock and Brock, 1971).

Thin sections, which were created for representative rock examples of fresh, surface-only alteration, and complete crust to core alteration, provided insights on the degree, extent, style and textures of alteration (Fig. 10). All samples have porphyritic textures with  $\leq 50$  vol.% phenocrysts contents. The fresh sample (tg12) had a very low porosity ( $\leq 5$  vol.%) and very little evidence of alteration that resulted in a flat spectral curve. In contrast, the higher porosity (10–20 vol.%) crust-altered (tg13) and pervasively altered sample (tg14) both show absorption features that are typical of clay minerals with OH in their crystal structures (Fig. 10). The SEM-BSE images show that the alteration is concentrated in the matrix and along the edges of mostly plagioclase phenocrysts (Fig. 10). The altered zones are characterised by high concentrations of Mg, Al, O and Si elements based on the EDS spot measurements, which is consistent with magnesium-rich and aluminium-rich silicate clays. The Al-rich end-members have been recognized as kaolinite and halloysite (general formula is  $\text{Al}_2\text{Si}_2\text{O}_5(\text{OH})_4$ ), while the Mg-rich end-member is montmorillonite (general formula is

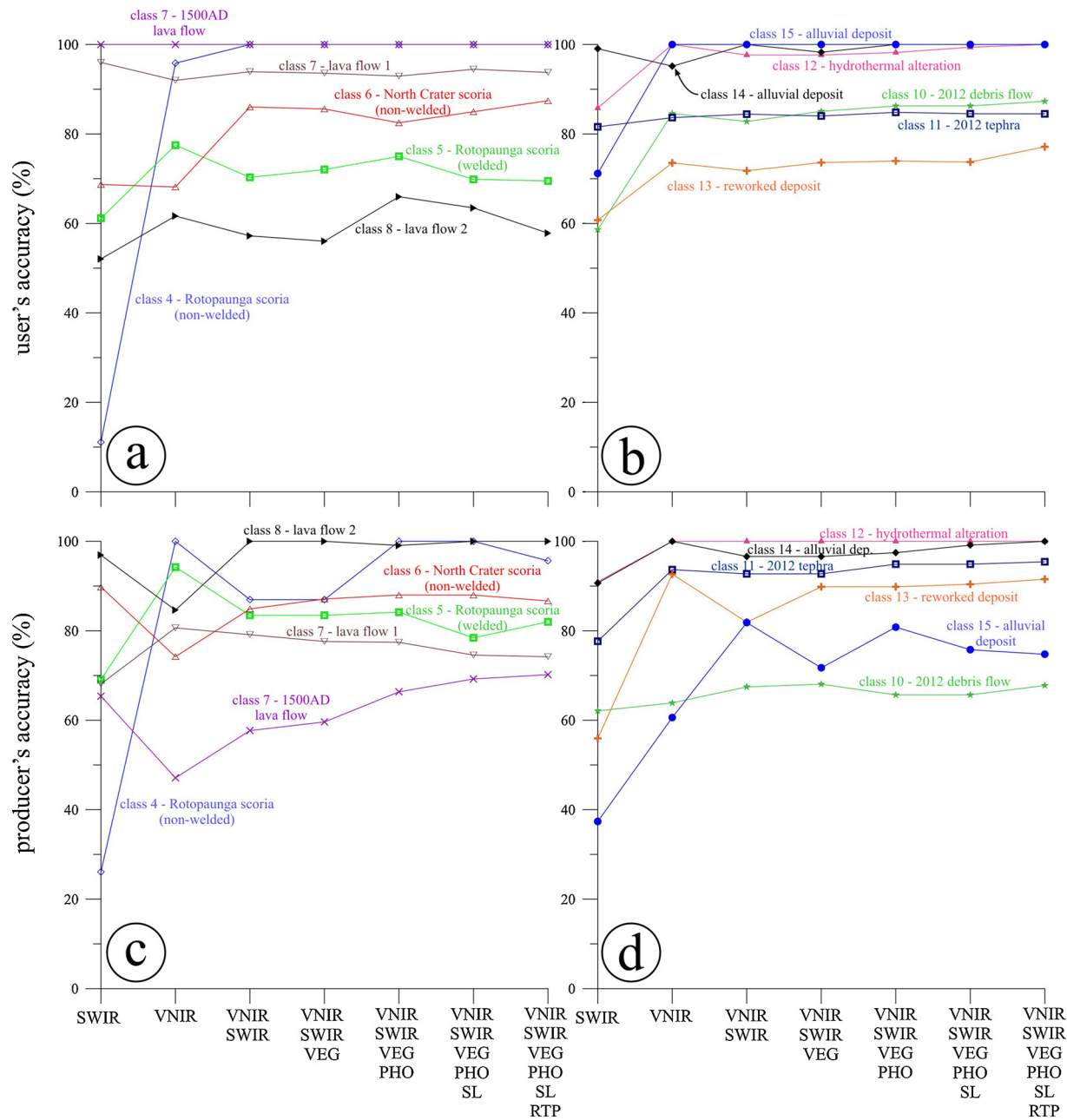


**Fig. 8.** User's and producer's accuracy measures as a function of different combination of image inputs with multi-scale texture maps.

$(\text{Na},\text{Ca})_{0.33}(\text{Al},\text{Mg})_2(\text{Si}_4\text{O}_{10})(\text{OH})_2 \times n\text{H}_2\text{O}$ . The EDS-based element maps are highly consistent with the laboratory-based spectroscopy results. Both methods indicate the presence of clay-minerals in a varying extent, which is shown to be linked to porosity (Julia et al., 2014; Wyering et al., 2014). A detailed discrimination of different clay mineral species could be confirmed with X-Ray Diffraction analysis, but is beyond the scope of this study.

#### 4. Discussion

##### 4.1. Surface geological mapping through image classification

Previous studies using the identical training data and classification algorithms found that Landsat 8 OLI and Sentinel 2A can provide image classification accuracies in the range of OA  $\sim$  57–69% (Keresztsuri et al., 2018). Hyperspectral data (e.g. OA = 77.6%) alone can only marginally outperform multispectral images for geological mapping

applications (Fig. 6), but this high spatial and spectra resolution data can deliver new information that multispectral satellites cannot provide (e.g. mineral species). Moreover, an improved image classification for mapping volcanic terrains needs additional supporting information that can be derived from axillary information (e.g. topographic data from LiDAR). This has improved the classification accuracy slightly (e.g. OA = 80.8%, Fig. 6). The biggest improvement, however, is achieved after including textural attributes of the MNF-bands into the classification workflow. This improved the accuracy by an additional 5% compared to the same dataset without textural attributes, reaching an overall accuracy of 85%. Therefore, these types of spatial and spectral datasets can provide high-resolution and accurate baseline information for volcano mapping.

The proposed approach is cost-effective and fast in providing updated geological maps from airborne, and even satellite platforms, for frequently active, and thus unsafe or inaccessible, volcanic areas globally. For broad-scale mapping considering only altered and non-

**Table 4**

Summary of the user's and producer's accuracy for the 15 classes.

Classes	User's Accuracy [%]				Producer's Accuracy [%]			
	Estimate	Standard Error	95 % Interval		Estimate	Standard Error	95 % Interval	
1 - vegetation (forest, scrub)	95.16	0.33	94.51	95.8	91.97	1.04	89.94	94.01
2 - dead vegetation	78.5	0.63	77.27	79.74	51.06	1.99	47.17	54.96
3 - shadow	98.23	0.2	97.83	98.63	94.87	1.13	92.65	97.1
4 - Rotopaunga scoria (non-welded)	100	0	100	100	95.65	4.15	87.52	103.79
5 - Rotopaunga scoria (welded)	69.51	0.71	68.13	70.89	82.01	2.88	76.36	87.66
6 - North Crater scoria (non-welded)	87.44	0.51	86.45	88.44	86.67	1.93	82.89	90.45
7 - lava flow 1 (North Crater)	93.76	0.37	93.04	94.49	74.19	1.52	71.22	77.17
8 - lava flow 2 (North Crater)	57.83	0.76	56.35	59.31	100	0	100	100
9 - 1500 AD lava flow (Te Maari)	100	0	100	100	70.19	3.63	63.08	77.3
10 - 2012 debris flow (Te Maari)	87.31	0.51	86.31	88.31	67.76	2.03	63.79	71.73
11 - 2012 tephra (Te Maari)	84.51	0.55	83.42	85.59	95.42	0.71	94.04	96.81
12 - hydrothermal alteration (Te Maari)	100	0	100	100	100	0	100	100
13 - reworked deposit (Te Maari)	77.14	0.64	75.88	78.4	91.53	2.01	87.59	95.46
14 - alluvial deposit (Blue & Sulphur Lakes)	100	0	100	100	100	0	100	100
15 - alluvial deposit (Ketetahi springs)	100	0	100	100	74.75	3.73	67.44	82.06

**Table 5**

Error matrix of the 15 classes used in this study.

Classes	Reference Class															Total
	1	2	3	4	5	6	7	8	9	10	11	12	13	14	15	
1 - vegetation (forest, scrub)	550	11	15	0	0	0	2	0	0	0	0	0	0	0	0	578
2 - dead vegetation	0	168	0	0	0	0	21	0	16	0	0	0	0	0	0	214
3 - shadow	0	0	333	0	0	0	0	0	0	4	0	0	2	0	0	339
4 - Rotopaunga scoria (non-welded)	0	0	0	22	0	0	0	0	0	0	0	0	0	0	0	22
5 - Rotopaunga scoria (welded)	0	2	0	0	114	30	6	0	12	0	0	0	0	0	0	164
6 - North Crater scoria (non-welded)	0	0	0	0	25	195	0	0	3	0	0	0	0	0	0	223
7 - lava flow 1 (North Crater)	1	21	0	0	0	0	391	0	0	0	0	0	0	0	4	417
8 - lava flow 2 (North Crater)	0	127	3	0	0	0	107	325	0	0	0	0	0	0	0	562
9 - 1500 AD lava flow (Te Maari)	0	0	0	0	0	0	0	0	73	0	0	0	0	0	0	73
10 - 2012 debris flow (Te Maari)	0	0	0	1	0	0	0	0	0	227	32	0	0	0	0	260
11 - 2012 tephra (Te Maari)	47	0	0	0	0	0	0	0	58	709	0	13	0	12	839	
12 - hydrothermal alteration (Te Maari)	0	0	0	0	0	0	0	0	0	0	166	0	0	0	0	166
13 - reworked deposit (Te Maari)	0	0	0	0	0	0	0	0	46	2	0	162	0	0	0	210
14 - alluvial deposit (Blue & Sulphur Lakes)	0	0	0	0	0	0	0	0	0	0	0	0	118	0	0	118
15 - alluvial deposit (Ketetahi springs)	0	0	0	0	0	0	0	0	0	0	0	0	0	74	74	74
Total	598	329	351	23	139	225	527	325	104	335	743	166	177	118	99	4259

altered classes, hyperspectral imagery can be substituted with multispectral satellite images to provide discrimination between spectrally active hydroxyl-bearing and Fe-bearing minerals. This can improve the applicability of the proposed workflow to other volcanoes without the need to acquire hyperspectral images. Additional improvements and data availability could be achieved through the addition of other remote sensing data, such as radar imagery (Pal et al., 2007), and/or geophysical data (Cracknell and Reading, 2014).

#### 4.2. Sedimentary processes and lithostratigraphy from hyperspectral imaging

This study shows that textural information from the hyperspectral imagery can provide proxies to improve recognition of lithologies even with a high degree of spectral similarity (e.g. reworked and in situ clay deposits, or agglutinated/welded and non-welded scoriaceous deposits). For example, Class 10 – debris flow deposits and Class 11 – tephra deposits are both direct products of the 2012 Te Maari hydrothermal eruptions and are largely made of the same lithologies (Pardo et al., 2014; Procter et al., 2014). The improved accuracy is due to the mainly textural features of the deposits (e.g. coarse grain-size and poor sorting of the debris flow deposits in contrast with lapilli and medium sorted appearance of the tephra fall deposits; Fig. 3C and D). This highlights the fact that hyperspectral imagery carries some genetic (e.g. sediment transport processes), lithostratigraphic (e.g. distinction of lava

flows surfaces with different age), and sedimentological information (e.g. grain size, sorting, and agglutination and welding). These are integrated indirectly into the spectral, topographic, and textural properties of the terrain. The deconvolution of such features in remotely sensed imagery can improve our understanding of geologic processes in active volcanic environments (e.g. surface age, lithostratigraphy and stratigraphic position).

#### 4.3. Mapping debris flow source zones

The mineral suites studied here are predominantly made of clay minerals (e.g. kaolinite, halloysite, illite, montmorillonite) and Fe-bearing oxidized minerals (e.g. goethite, hematite). These minerals form due to in situ hydrothermal alteration from underground fluids and from water infiltrating from the surface. It is important to note that hydrothermally altered deposits can be transported away its source (e.g. through debris flows, and fluvial activity), or can continue to alter in a distal position due to interaction with meteoric fluids. Spectrally, however, these lithologies are very similar, preventing accurate spatial mapping and distinction between them. The improved mapping of reworking processes of hydrothermally altered deposits was enabled through image textures in this study (e.g. Class 13 and 14 in Figs. 7 and 8).

The derived surface geological map shows 4 classes (e.g. Class 12–15) that are made of hydrothermally altered deposits (Fig. 5). One

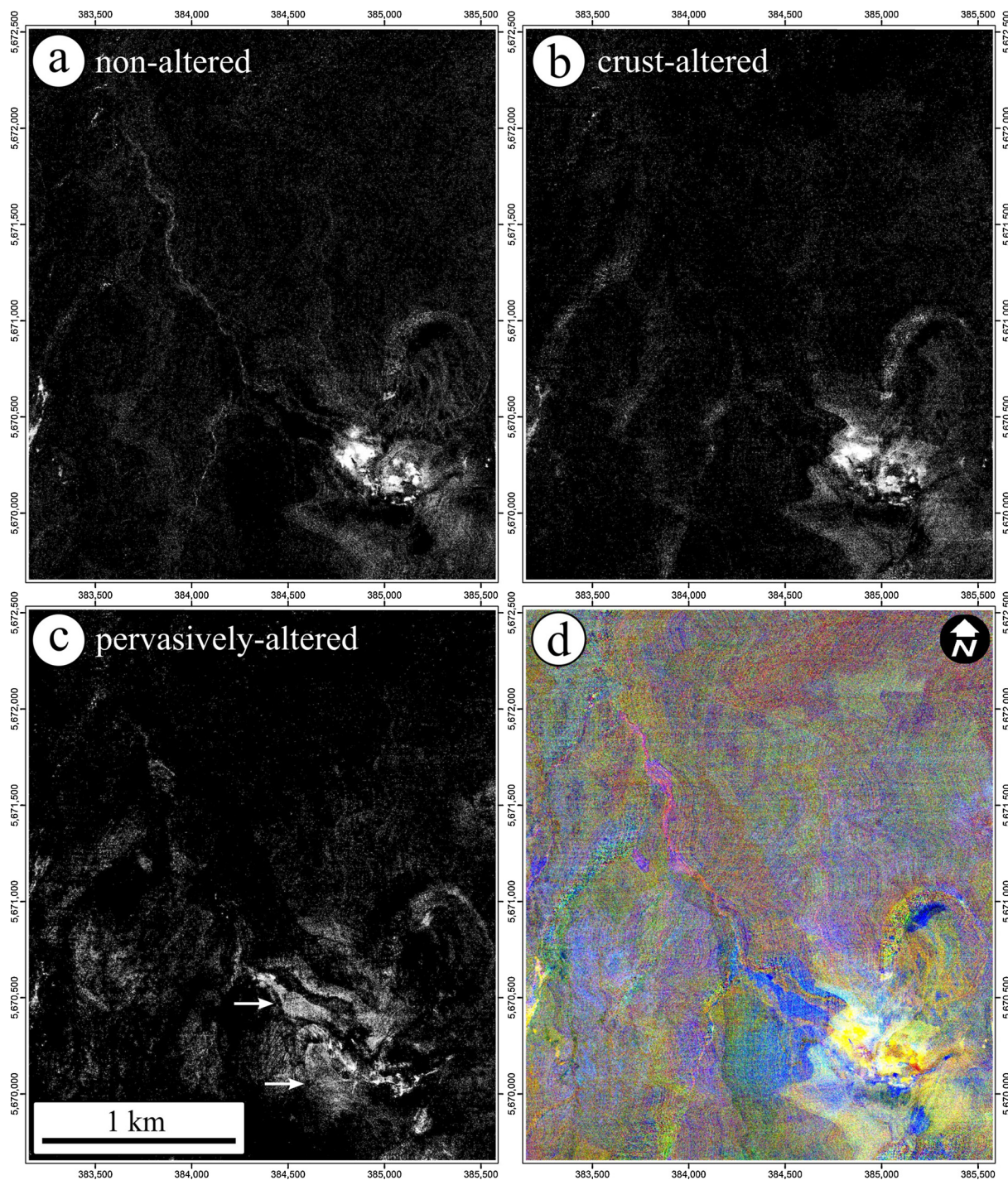


**Fig. 9.** End-member matching using for airborne imagery: (A) fresh, non-altered, (B) crust-type alteration, and (C) pervasively altered samples. The white colour shows good matching while the black pixel represents poor matching. The white horizontal arrows show the spatial distribution of tephra deposits rather than the pervasively altered in situ deposits. (D) RGB composite of the three end-member matching images.

class is in situ and 3 classes are reworked by alluvial processes from various sources. Based on the spatial distribution of hydrothermally alteration deposits, a first-order map of potential debris flow source areas can be developed (Fig. 11). The total area of alteration mapped here is  $0.43 \text{ km}^2$ , concentrated around Ketetahi springs and Te Maari craters (Fig. 11). In comparison, satellite-based mapping shows alteration present over an area of  $0.53 \text{ km}^2$  (Keresztsuri et al., 2018). This measured extent is an order of magnitude larger area than the source area of the 2012 debris flow (Procter et al., 2014). This shows the Te Maari area has still substantial hydrothermally altered regions to

produce similar debris flow in the future.

#### 4.4. Assessing surface and sub-surface hydrothermal alteration remotely

One challenge of hydrothermal alteration mapping from remote sensing is that it only acquires surface measurements, as the light does not penetrate the substrate. Consequently, hydrothermal alteration could be only superficial (e.g. Fig. 10), potentially leading to an overestimation of the overall alteration through remote sensing. Through spectral matching, the fresh and crust altered areas can be easily recognized

**Table 6**  
Type of minerals detected in the sample using laboratory-based spectroscopy. The score of SAM + SFF is a dimension less number in which perfect match is 2. Abbreviation: SAM – Spectral Angle Mapper, SFF – Spectral Fitting Function.

sample ID	Description	Mineral groups	Mineralogy	SAM + SFF score
tg01	Sand to silt sized alluvium with variously altered scoria, lava rocks fragment, and pumice	phyllosilicates and tectosilicates	rectorite ± clinoptilolite ± mordenite	1.957
tg02	Sand to silt sized alluvium with variously altered scoria, lava rocks fragment, and pumice	phyllosilicates	montmorillonite ± sepiolite ± rectorite	1.939
tg03	mm-scaled white to grey crust with larger coarse lapilli to block sized fragements, local enrichment of sulphur crust	phyllosilicates and oxides	montmorillonite ± hyalite ± palygorskite	1.947
tg04	mm-scaled white to grey crust with larger coarse lapilli to block sized fragements, local enrichment of sulfur crust	phyllosilicates and tectosilicates	rectorite ± hectorite ± orthoclase	1.939
tg05	highly altered dark silt sized deposit	–	good match with only spectrally featureless minerals	–
tg06	slightly altered scorieous deposit with coarse lapillit to block grain size	–	discarded	–
tg07	Yellow, pale, bluish clay alteration	phyllosilicates and tectosilicates	clinopilolite ± mordenite ± montmorillonite	1.928
tg08	coarse to medium lapilli deposits from the 2012 eruption in proximal position	tectosilicate	microcline ± perthite	1.892
tg09	coarse to medium lapilli deposits from the 2012 eruption in proximal position	phyllosilicates, tectosilicates and sulfates	rectorite ± thennardite ± microcline	1.911
tg10	highly altered, yellow, white to pink slightly lithified volcanicic sediments	phyllosilicates, tectosilicates and sulfates	rectorite ± thennardite ± hectorite ± clinoptilolite	1.921
tg11	yellow to grey clay horizon beneath the debris flow deposits	phyllosilicates and tectosilicates	clinopilolite ± montmorillonite ± mordenite	1.928
tg12crust	freshly-looking sample of lava rocks with porphyritic texture	primary minerals	–	–
tg12interior	freshly-looking sample of lava rocks with porphyritic texture	primary minerals	discarded	–
tg13crust	lava rock with surface alteration crust and fresh interour	primary minerals, and phyllosilicates, tectosilicates, sulfates detected on the rim	montmorillonite ± endellite ± kaolinite	1.697
tg13interior	lava rock with surface alteration crust and fresh interour	primary minerals, and phyllosilicates, tectosilicates, sulfates detected on the rim	halloysite ± kaolinite ± nacrite	1.671
tg14crust	pervasively altered welded scoria deposit	phyllosilicates and tectosilicates	nontronite ± montmorillonite ± endellite	1.69
tg14interior	pervasively altered welded scoria deposit	phyllosilicates and tectosilicates	kaolinite ± montmorillonite ± halloysite	1.601

(Fig. 9). These lithologies are mapped to be distributed over the same area (Fig. 9A and B) shows that this workflow can be useful to recognize “false-positive” hydrothermally altered areas in a volcanic setting. In contrast, the pervasively altered rocks have falsely been mapped in places by spectral matching algorithm (Fig. 9C). This is due to the fact that the pervasively altered lithology has been remobilized by both landslide/debris flow and 2012 lateral blasts from Upper Te Maari. This resulted in an overestimation of the pervasively altered areas.

To extend the capability of hyperspectral imaging, the spectral data can be used in conjunction with ground data (e.g. physical properties of the surface and subsurface lithologies). A similar approach was recently introduced to map macro- and micro-element concentrations and physical properties of vegetation (Pullanagari et al., 2016; Yule et al., 2016; Pullanagari et al., 2017). In a volcanic context, various physical properties of outcropping rocks can be measured in situ, such as strength and porosity, which in turn can provide input to develop predictive models using hyperspectral imaging. Physical property maps (i.e. geotechnical maps) can provide important inputs for numerical modelling and volcanic hazard assessments. Similarly, geophysical imaging techniques, such as gravity and aero-magnetic data (e.g. Finn et al., 2018) can be correlated with spectral signals, providing a new technique to image a volcano’s architecture and geology. These spectral mapping applications with various physical or geophysical surface and subsurface properties of a volcano warrants future investigations.

#### 4.5. Spectral volcanology –future perspectives and limitations

Spatial variations in hydrothermal alteration of volcanic rocks over time might hold important clues to the volcano’s evolution. This information can be used to predict the short and long-term behaviour of volcanoes (e.g. fluid circulation zones, structural weakness zones, degassing patterns), contributing to better forecasting of geological hazards. Airborne platforms for this purpose can make data acquisition very flexible compared to fixed satellite overpass. Moreover, this platform can provide multi-temporal image acquisition, which can be used to track volcanic processes over time (e.g. tephra deposition, landslide activity, hydrothermal alteration and geothermal activity). This technology can additionally be used to build up a spectral library of volcanic terrains, which can keep track of erosional (e.g. debris flow and landslide activity), depositional processes (e.g. lava flow emplacement, tephra deposition), and in-situ hydrothermal alteration. The optical imagery from hyperspectral missions can be further improved by image fusion with high-resolution topographic information to highlight elevation changes, such as post-lahar (Procter et al., 2010) and lava flow emplacement (Bagnardi et al., 2016). This all points toward the need for a better uptake of hyperspectral imaging within the volcanological community.

Developing new utilizations of hyperspectral remote sensing to map and monitor active volcanic areas is an important direction of future research. The launch of the new generation of hyperspectral satellite missions, such as EnMAP (Guanter et al., 2015), HISUI (Matsumaga et al., 2015), HysIRI (Lee et al., 2015) and PRISMA (Stefano et al., 2013), will provide a more frequent temporal repeat time of 1–4 weeks with a medium spatial resolution (e.g. ~30 m). The joint use of several remotely sensed platforms (e.g. airborne and spaceborne hyperspectral, LiDAR, and geophysical data) can improve the identification of altered areas more susceptible to failure (Kluger et al., 2017) and map evolving hazards as they form during an on-going volcanic crisis. The development of a new generation of data analytics on hyperspectral remote sensing for geological application should be developed before spaceborne hyperspectral missions. The Tongariro Volcanic Complex, with its high-resolution airborne hyperspectral base line imagery, can be used as a future method development, ground calibration, and validation site for future spaceborne satellite missions.

The limitations of hyperspectral imaging include snow/ice and/or vegetation covers, such as scrub, lichen and moss fraction that can

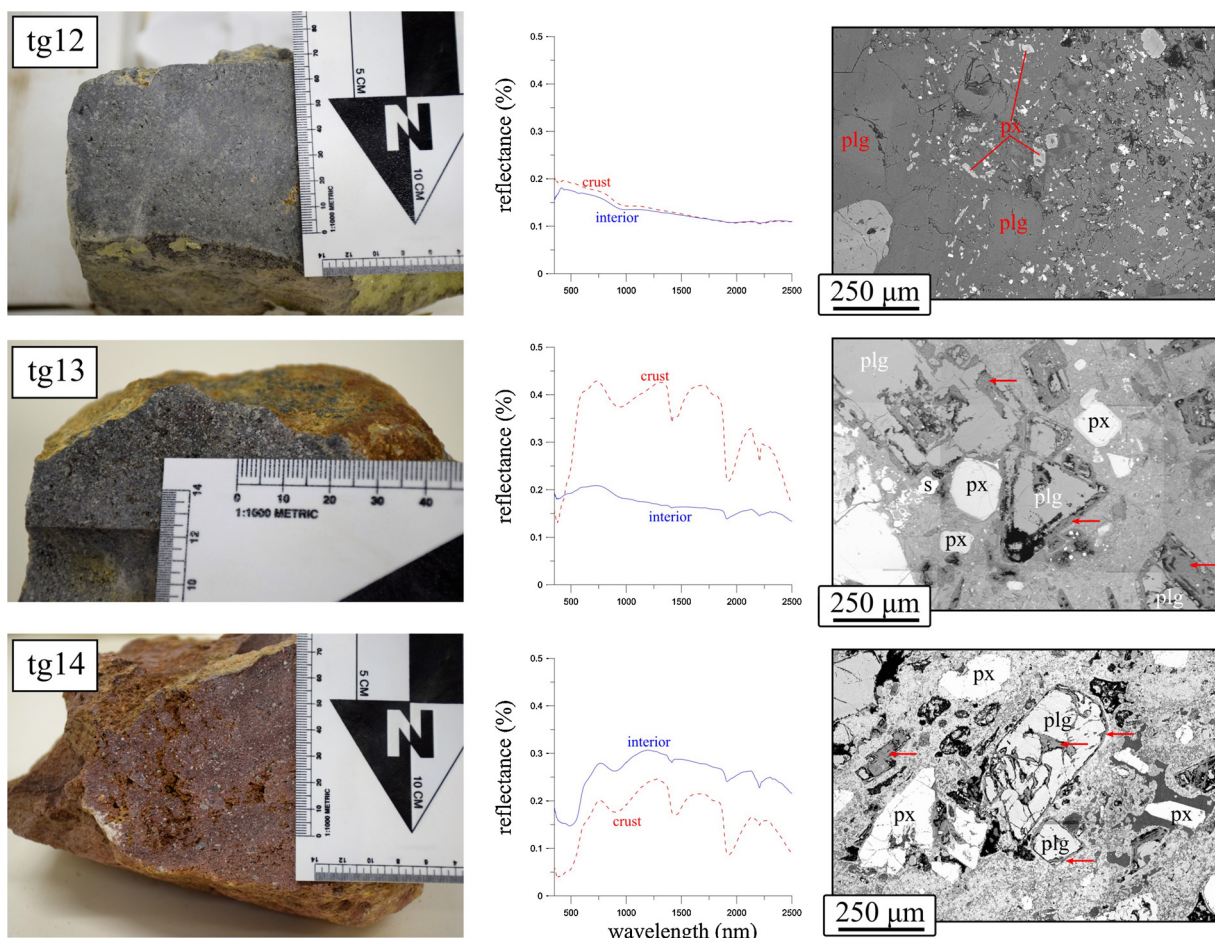


**Fig. 10.** Representative hydrothermal alteration end-members from the Te Maari craters: (tg12) fresh lava rocks, (tg13) crust-alteration with fresh interior and (tg14) pervasively altered and oxidized lava rocks. The figure shows the photo of the hand specimen, spectral reflectance from spectroscopy, gray-scale BSE images. Note the complete to partial clay-alteration around crystals, such as plagioclase (red arrows). Abbreviations: px – pyroxene, plg – plagioclase, s – sulphur, tm – titanomagnetite.

contaminate the bare ground light reflectance. This eliminates volcanoes with permanent ice cover (e.g. Deception Island, Antarctica), and winter acquisitions (e.g. Mt Ruapehu, New Zealand). However, vegetation analysis from remotely sensed images can also provide useful insights, such as volcano degassing and/or tephra fall that can cause vegetation die-off (Tortini et al., 2017). This is particularly applicable for areas of high agricultural use. At the Te Maari craters, some of the older lava flows (e.g. Class 7 and 8) and scoria deposits (Class 4–6) have a relatively low recognition around 60–80% (Figs. 7 and 8), which may be partially explained by vegetation cover. Lichen, in particular, can cause shifts in absorption features of typical mineral in the SWIR region (Salehi et al., 2017), leading image classification efforts to fail. However, volcanic units, such as lava flows, might have a predictable lichen cover as they age (e.g. Li et al., 2015). Lichen cover exists in tandem with the chemical and mechanical weathering of the lava flow surfaces, making older lava flows more abundant in soil and fine-grained particles ( $\leq 2$  cm), which might be good proxies for dating geological surfaces using spectral information (e.g. Crouvi et al., 2006).

## 5. Conclusions

Imaging volcanic terrains using hyperspectral remote sensing, along with other high-resolution optical and topographic data (e.g. LiDAR), can contribute to a semi-automated classification method for geological

surface mapping. This classification relies on the combination of spectral information from hyperspectral imagery and topographic information from LiDAR to recognize geological and geomorphologic features on volcanoes and to infer surface processes from imagery. The use of hyperspectral remote sensing can recognize different lithologies quantitatively in the spatial and spectral dimensions as well as terrain position, morphology, surface roughness, and bulk composition from spectral signatures.

Spectral imaging data is useful for both mapping the spatial extent and identifying individual mineral species using their reflected light properties. Thus, this type of dataset is extremely valuable as a first order reconnaissance tool for detailed mapping projects to understand the spatial distribution of lithologies in a volcanic system. The practical implication of volcano mapping is the improved mapping of hazardous phenomena (in our case study, debris flow sources areas) that can be used as an input for numerical modelling of debris flows and volcanic hazard assessment.

We suggest that our methodology could be used as a monitoring tool, whereby a time series of airborne surveys could track the shifting focus of hydrothermal activity. This can highlight dynamically changing area of an active volcano over time, aiding hazard mitigation and assessment efforts. This new remote sensing capability makes it possible to understand volcano behavior and processes on a short-time scale, allowing a vital step toward near-real time volcano surveillance.

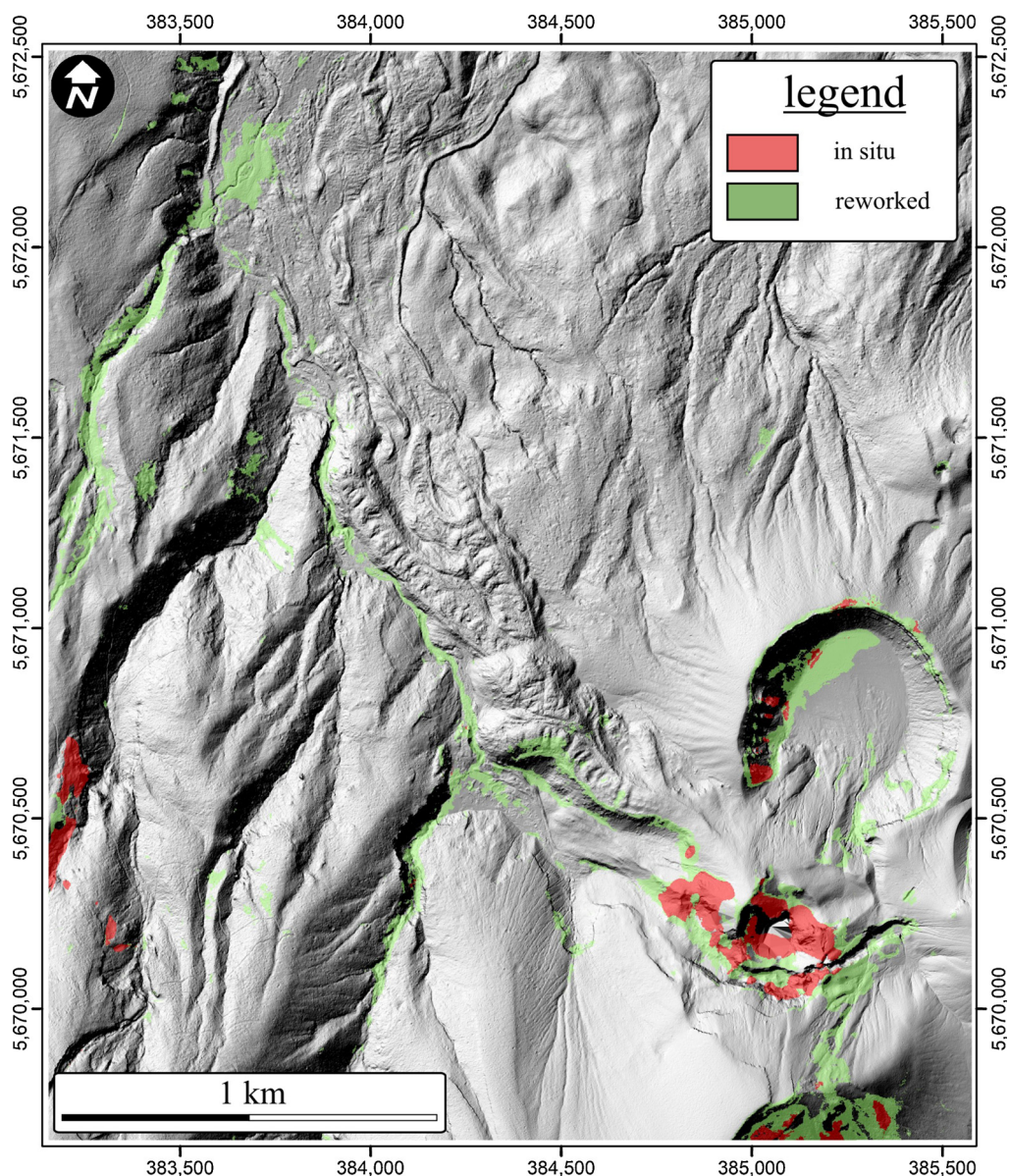


**Fig. 11.** In situ (red) and reworked deposits (green) with presence of clay minerals identified through image classification.

## Acknowledgments

This study was supported by Early Career Researchers Fund from the College of Science, Massey University. It was also partially supported by Natural Hazards Research Platform (“Too big to fail? – A multidisciplinary approach to predict collapse and debris flow hazards from Mt. Ruapehu”) and the National Science Foundation (grant number: 1714054).

The authors are grateful for the support from Aerial Survey Ltd for the image acquisition, and Specim Ltd. for support on image processing. The image data used in this paper, including LiDAR and aerial imagery, are in the public domain. It can be accessed after registration from the Land Information New Zealand’s website (<https://www.linz.govt.nz/data/linz-data-service>). The hyperspectral image data of Te Maari craters is available for download through the Vhub.org website (<https://vhub.org/resources/4375>) for future method development studies on image classification.

## Appendix A. Supplementary data

Supplementary material related to this article can be found, in the online version, at <https://doi.org/10.1016/j.jag.2018.07.006>.

## References

- Bagnardi, M., González, P.J., Hooper, A., 2016. High-resolution digital elevation model from tri-stereo pleiades-1 satellite imagery for lava flow volume estimates at Fogo Volcano. *Geophys. Res. Lett.* 43 (12), 6267–6275.
- Bedini, E., van der Meer, F., van Ruitenbeek, F., 2009. Use of HyMap imaging spectrometer data to map mineralogy in the Rodalquilar caldera, southeast Spain. *Int. J. Remote Sens.* 30 (2), 327–348.
- Behncke, B., Fornaciai, A., Neri, M., Favalli, M., Ganci, G., Mazzarini, F., 2016. Lidar surveys reveal eruptive volumes and rates at Etna, 2007–2010. *Geophys. Res. Lett.* 43 (9), 4270–4278.
- Belgiu, M., Drăguț, L., 2016. Random forest in remote sensing: a review of applications and future directions. *ISPRS J. Photogramm. Remote Sens.* 114, 24–31.
- Bibby, H.M., Caldwell, T.G., Davey, F.J., Webb, T.H., 1995. Geophysical evidence on the structure of the Taupo Volcanic Zone and its hydrothermal circulation. *J. Volcanol. Geotherm. Res.* 68 (1), 29–58.
- Boardman, J.W., Kruse, F.A., Green, R.O., 1995. Mapping target signatures via partial

- unmixing of AVIRIS data, summaries. Proceedings of the Fifth JPL Airborne Earth Science Workshop. JPL Publication, Pasadena, California.
- Breiman, L., 2001. Random forests. *Mach. Learn.* 45 (1), 5–32.
- Brock, T.D., Brock, M.L., 1971. Microbiological studies of thermal habitats of the central volcanic region, North Island, New Zealand. *N. Z. J. Mar. Freshw. Res.* 5 (2), 233–258.
- Carrino, T.A., Cróstá, A.P., Toledo, C.L.B., Silva, A.M., 2018. Hyperspectral remote sensing applied to mineral exploration in southern Peru: A multiple data integration approach in the Chapi Chiara gold prospect. *Int. J. Appl. Earth Obs. Geoinf.* 64, 287–300.
- Chen, J.M., Leblanc, S.G., Miller, J.R., Freemantle, J., Loeschel, S.E., Walthall, C.L., Innanen, K.A., White, H.P., 1999. Compact airborne spectrographic imager (CASI) used for mapping biophysical parameters of boreal forests. *J. Geophys. Res.* 104 (D22), 27945–27958.
- Clark, R.N., 1999. Chapter 1: spectroscopy of Rocks and minerals, and principles of spectroscopy. In: Rencz, A. (Ed.), *Manual of Remote Sensing - Remote Sensing for the Earth Sciences*. John Wiley and Sons, Inc, New York, USA, pp. 3–58.
- Clark, R.N., Swazye, G.A., Wise, R., Livo, E., Hoefen, T., Kokaly, R., Sutley, S.J., 2007. USGS Digital Spectral Library splib06a. U.S. Geological Survey Digital Data Series 231.
- Cracknell, M.J., Reading, A.M., 2014. Geological mapping using remote sensing data: a comparison of five machine learning algorithms, their response to variations in the spatial distribution of training data and the use of explicit spatial information. *Comput. Geosci.* 63 (0), 22–33.
- Crouvi, O., Ben-Dor, E., Beyth, M., Avigad, D., Amit, R., 2006. Quantitative mapping of arid alluvial fan surfaces using field spectrometer and hyperspectral remote sensing. *Remote Sens. Environ.* 104 (1), 103–117.
- Crowley, J.K., Hubbard, B.E., Mars, J.C., 2003a. Analysis of potential debris flow source areas on Mount Shasta, California, by using airborne and satellite remote sensing data. *Remote Sens. Environ.* 87 (2–3), 345–358.
- Crowley, J.K., Williams, D.E., Hammarstrom, J.M., Piatak, N., Chou, I.-M., Mars, J.C., 2003b. Spectral reflectance properties (0.4–2.5 μm) of secondary Fe-oxide, Fe-hydroxide, and Fe-sulphate-hydrate minerals associated with sulphide-bearing mine wastes. *Geochim. Explor. Environ. Anal.* 3 (3), 219–228.
- Crowley, J.K., Zimbelman, D.R., 1997. Mapping hydrothermally altered rocks on Mount Rainier, Washington, with Airborne Visible/Infrared imaging spectrometer (AVIRIS) data. *Geology* 25 (6), 559–562.
- De Boissieu, F., Sevin, B., Cudahy, T., Mangeas, M., Chevrel, S., Ong, C., Rodger, A., Maurizot, P., Laukamp, C., Lau, I., Touraivane, T., Cluzel, D., Despinoy, M., 2018. Regolith-geology mapping with support vector machine: A case study over weathered Ni-bearing peridotites, New Caledonia. *Int. J. Appl. Earth Obs. Geoinf.* 64, 377–385.
- Feng, J., Rogge, D., Rivard, B., 2018. Comparison of lithological mapping results from airborne hyperspectral VNIR-SWIR, LWIR and combined data. *Int. J. Appl. Earth Obs. Geoinf.* 64, 340–353.
- Finn, C.A., Desczcz-Pan, M., Ball, J.L., Bloss, B.J., Minsley, B.J., 2018. Three-dimensional geophysical mapping of shallow water saturated altered rocks at Mount Baker, Washington: implications for slope stability. *J. Volcanol. Geotherm. Res.* 357, 261–275.
- Forzieri, G., Tanteri, L., Moser, G., Catani, F., 2013. Mapping natural and urban environments using airborne multi-sensor ADS40–MIVIS–LiDAR synergies. *Int. J. Appl. Earth Obs. Geoinf.* 23, 313–323.
- Goetz, A.F.H., Vane, G., Solomon, J.E., Rock, B.N., 1985. Imaging spectrometry for Earth remote sensing. *Science* 228 (4704), 1147–1153.
- Gómez-Vasconcelos, G.M., Villamor, P., Cronin, S.J., Procter, J., Keresztsuri, G., Palmer, A., Townsend, D., Leonard, G., Berryman, K., Ashraf, S., 2016. Earthquake history at the eastern boundary of South Taupo Volcanic Zone, New Zealand. *N. Z. J. Geol. Geophys.* 59 (4), 522–543.
- Green, A.A., Berman, M., Switzer, P., Craig, M.D., 1988. A transformation for ordering multispectral data in terms of image quality with implications for noise removal. *Geosci. Remote Sens., IEEE Trans.* 26 (1), 65–74.
- Guanter, L., Kaufmann, H., Segl, K., Foerster, S., Rogass, C., Chabirillat, S., Kuester, T., Hollstein, A., Rossner, G., Chlebek, C., Straif, C., Fischer, S., Schrader, S., Storch, T., Heiden, U., Mueller, A., Bachmann, M., Mühlé, H., Müller, R., Habermeyer, M., Ohndorf, A., Hill, J., Buddenbaum, H., Hostert, P., van der Linden, S., Leitão, P., Rabe, A., Doerner, R., Krasemann, H., Xi, H., Mauser, W., Hank, T., Locherer, M., Rast, M., Staenz, K., Sang, B., 2015. The EnMAP spaceborne imaging spectroscopy Mission for earth observation. *Remote Sens.* 7 (7), 8830.
- Guinness, E.A., Arvidson, R.E., Jolliff, B.L., Seelos, K.D., Seelos, F.P., Ming, D.W., Morris, R.V., Graff, T.G., 2007. Hyperspectral reflectance mapping of cinder cones at the summit of mauna kea and implications for equivalent observations on Mars. *J. Geophys. Res.* 112 (E8), E08S11.
- Hamilton, V.E., Morris, R.V., Gruener, J.E., Mertzman, S.A., 2008. Visible, near-infrared, and middle infrared spectroscopy of altered basaltic tephra: spectral signatures of phyllosilicates, sulfates, and other aqueous alteration products with application to the mineralogy of the Columbia Hills of Gusev Crater, Mars. *J. Geophys. Res.* 113 (E12), E12S43.
- Haralick, R.M., Shanmugam, K., Dinstein, I., 1973. Textural features for image classification. *IEEE Transactions on Systems, Man, and Cybernetics, SMC-3(6)* 610–621.
- Hellman, M.J., Ramsey, M.S., 2004. Analysis of hot springs and associated deposits in yellowstone national Park using ASTER and AVIRIS remote sensing. *J. Volcanol. Geotherm. Res.* 135.
- Hobden, B.J., Houghton, B.F., Lanphere, M.A., Nairn, I.A., 1996. Growth of the tongariro volcanic complex: New evidence from K-Ar age determinations. *N. Z. J. Geol. Geophys.* 39 (1), 151–154.
- Hobden, B.J., Houghton, B.F., Davidson, J.P., Weaver, S.D., 1999. Small and short-lived magma batches at composite volcanoes: time windows at Tongariro volcano, New Zealand. *J. Geol. Soc. Lond.* 156 (5), 865–868.
- Hobden, B., Houghton, B., Nairn, I., 2002. Growth of a young, frequently active composite cone: Ngauruhoe volcano, New Zealand. *Bull. Volcanol.* 64 (6), 392–409.
- Hosseini Zadeh, M., Tangestani, M.H., Roldan, F.V., Yusta, I., 2014. Sub-pixel mineral mapping of a porphyry copper belt using EO-1 Hyperion data. *Adv. Space Res.* 53 (3), 440–451.
- Houghton, B.F., Wilson, C.J.N., McWilliams, M.O., Lanphere, M.A., Weaver, S.D., Briggs, R.M., Pringle, M.S., 1995. Chronology and dynamics of a large silicic magmatic system: Central Taupo Volcanic Zone, New Zealand. *Geology* 23, 13–16.
- Huesca, M., García, M., Roth, K.L., Casas, A., Ustin, S.L., 2016. Canopy structural attributes derived from AVIRIS imaging spectroscopy data in a mixed broadleaf/conifer forest. *Remote Sens. Environ.* 182, 208–226.
- Jolly, A.D., Lokmer, I., Kennedy, B., Keys, H.J.R., Proctor, J., Lyons, J.J., Jolly, G.E., 2014. Active seismic sources as a proxy for seismic surface processes: an example from the 2012 Tongariro volcanic eruptions, New Zealand. *J. Volcanol. Geotherm. Res.* 286, 317–330.
- Julia, F., Vladimir, L., Sergey, R., David, Z., 2014. Effects of hydrothermal alterations on physical and mechanical properties of rocks in the Kuril–Kamchatka island arc. *Eng. Geol.* 183, 80–95.
- Keresztsuri, G., Németh, K., 2016. Sedimentology, eruptive mechanism and facies architecture of basaltic scoria cones from the Auckland Volcanic Field (New Zealand). *J. Volcanol. Geotherm. Res.* 324, 41–56.
- Keresztsuri, G., Procter, J., Cronin, S.J., Németh, K., Bebbington, M., Lindsay, J., 2012. LiDAR-based quantification of lava flow susceptibility in the City of Auckland (New Zealand). *Remote Sens. Environ.* 125, 198–213.
- Keresztsuri, G., Pullanagari, R.R., Mead, S., Schaefer, L.N., Procter, J., Schleiffarth, W.K., Kennedy, B., 2018. Geological mapping of hydrothermal alteration on volcanoes from multi-sensor platforms. 2018 IEEE International Geoscience and Remote Sensing Symposium (IGARSS). pp. 1–4.
- Kluger, M.O., Moon, V.G., Kreiter, S., Lowe, D.J., Churchman, G.J., Hepp, D.A., Seibel, D., Jorat, M.E., Mörz, T., 2017. A new attraction-detachment model for explaining flow sliding in clay-rich tephra. *Geology* 45 (2), 131–134.
- Kruse, F.A., 2012. Mapping surface mineralogy using imaging spectrometry. *Geomorphology* 137 (1), 41–56.
- Kruse, F.A., Lefkoff, A.B., Dietz, J.B., 1993. Airborne imaging spectrometry expert system-based mineral mapping in northern death valley, California/Nevada, using the airborne Visible/Infrared imaging spectrometer (AVIRIS). *Remote Sens. Environ.* 44 (2), 309–336.
- Kruse, F.A., Bedell, R.L., Tarani, J.V., Peppin, W.A., Weatherbee, O., Calvin, W.M., 2012. Mapping alteration minerals at prospect, outcrop and drill core scales using imaging spectrometry. *Int. J. Remote Sens.* 33 (6), 1780–1798.
- Kunkel, B., Blechinger, F., Viehmann, D., Piepen, H.V.D., Doerner, R., 1991. ROSIS imaging spectrometer and its potential for ocean parameter measurements (airborne and space-borne). *Int. J. Remote Sens.* 12 (4), 753–761.
- Lee, C.M., Cable, M.L., Hook, S.J., Green, R.O., Ustin, S.L., Mandl, D.J., Middleton, E.M., 2015. An introduction to the NASA Hyperspectral InfraRed Imager (HypIRI) mission and preparatory activities. *Remote Sens. Environ.* 167, 6–19.
- Li, L., Solana, C., Canters, F., Chan, J., Kervyn, M., 2015. Impact of environmental factors on the spectral characteristics of lava surfaces: field spectrometry of basaltic lava flows on Tenerife, Canary Islands. Spain. *Remote Sens.* 7 (12), 15864.
- Liu, C., Frazier, P., Kumar, L., 2007. Comparative assessment of the measures of thematic classification accuracy. *Remote Sens. Environ.* 107 (4), 606–616.
- Liu, L., Feng, J., Rivard, B., Xu, X., Zhou, J., Han, L., Yang, J., Ren, G., 2018. Mapping alteration using imagery from the Tiangong-1 hyperspectral spaceborne system: example for the Jintanzi gold province, China. *Int. J. Appl. Earth Obs. Geoinf.* 64, 275–286.
- Lombardo, V., Harris, A.J.L., Calvari, S., Buongiorno, M.F., 2009. Spatial variations in lava flow field thermal structure and effusion rate derived from very high spatial resolution hyperspectral (MIVIS) data. *J. Geophys. Res.: Solid Earth* 114 B02208.
- Magendran, T., Sanjeevi, S., 2014. Hyperion image analysis and linear spectral unmixing to evaluate the grades of iron ores in parts of Noamundi, Eastern India. *Int. J. Appl. Earth Obs. Geoinf.* 26, 413–426.
- Matsunaga, T., Iwasaki, A., Tsuchida, S., Tanii, J., Kashimura, O., Nakamura, R., Yamamoto, H., Tachikawa, T., Rokugawa, S., 2015. Hyperspectral imager suite (HSUI). Optical Payloads for Space Missions. John Wiley & Sons, Ltd, pp. 215–222.
- Mia, B., Fujimitsu, Y., 2012. Mapping hydrothermal altered mineral deposits using landsat 7 ETM+ image in and around Kuju volcano, Kyushu, Japan. *J. Earth Syst. Sci.* 121 (4), 1049–1057.
- Miller, C.A., Williams-Jones, G., 2016. Internal structure and volcanic hazard potential of Mt Tongariro, New Zealand, from 3D gravity and magnetic models. *J. Volcanol. Geotherm. Res.* 319, 12–28.
- Miller, C.A., Currenti, G., Hamling, I., Williams-Jones, G., 2018. Mass transfer processes in a post eruption hydrothermal system: parameterisation of microgravity changes at Te Maari craters, New Zealand. *J. Volcanol. Geotherm. Res.* 357, 39–55.
- Miyoshi, Y., Ishibashi, J.-i., Faure, K., Maeto, K., Matsukura, S., Omura, A., Shimada, K., Sato, H., Sakamoto, T., Uehara, S., Chiba, H., Yamanaka, T., 2013. Mg-rich clay mineral formation associated with marine shallow-water hydrothermal activity in an arc volcanic caldera setting. *Chem. Geol.* 355, 28–44.
- Montanaro, C., Scheu, B., Cronin, S.J., Beard, E.C.P., Lube, G., Dingwell, D.B., 2016. Experimental estimates of the energy budget of hydrothermal eruptions: Application to 2012 Upper Te Maari eruption, New Zealand. *Earth and Planet. Sci. Lett.* 452, 281–294.
- Moore, P.R., Brock, J.L., 1981. A physical and chemical survey of Ketetahi Hot Springs, Mt Tongariro, New Zealand. *New Zealand J. Sci.* 24 (2), 161–177.
- Mountrakis, G., Im, J., Ogole, C., 2011. Support vector machines in remote sensing: a review. *ISPRS J. Photogramm. Remote Sens.* 66 (3), 247–259.

- Murphy, R.J., Monteiro, S.T., 2013. Mapping the distribution of ferric iron minerals on a vertical mine face using derivative analysis of hyperspectral imagery (430–970 nm). *ISPRS J. Photogramm. Remote Sens.* 75, 29–39.
- Nairn, I.A., Kobayashi, T., Nakagawa, M., 1998. The ~10 ka multiple vent pyroclastic eruption sequence at tongariro volcanic Centre, taupo volcanic zone, New Zealand: part 1. Eruptive processes during regional extension. *J. Volcanol. Geotherm. Res.* 86 (1–4), 19–44.
- Nakagawa, M., Nairn, I.A., Kobayashi, T., 1998. The ~10 ka multiple vent pyroclastic eruption sequence at tongariro volcanic Centre, taupo volcanic zone, New Zealand: part 2. Petrological insights into magma storage and transport during regional extension. *J. Volcanol. Geotherm. Res.* 86 (1–4), 45–65.
- Pal, S.K., Majumdar, T.J., Bhattacharya, A.K., 2007. ERS-2 SAR and IRS-1C LISS III data fusion: a PCA approach to improve remote sensing based geological interpretation. *ISPRS J. Photogramm. Remote Sens.* 61 (5), 281–297.
- Pardo, N., Cronin, S.J., Németh, K., Brenna, M., Schipper, C.I., Beard, E., White, J.D.L., Procter, J., Stewart, B., Agustín-Flores, J., Moebis, A., Zernack, A., Keresztsuri, G., Lube, G., Auer, A., Neall, V., Wallace, C., 2014. Perils in distinguishing phreatic from phreatomagmatic ash: Insights into the eruption mechanisms of the 6 August 2012 Mt. Tongariro eruption, New Zealand. *J. Volcanol. Geotherm. Res.* 286, 397–414.
- Pieri, D., Abrams, M., 2004. ASTER watches the world's volcanoes: a new paradigm for volcanological observations from orbit. *J. Volcanol. Geotherm. Res.* 135, 13–28.
- Plaza, A., Benediktsson, J.A., Boardman, J.W., Brazile, J., Bruzzone, L., Camps-Valls, G., Chanussot, J., Fauvel, M., Gamba, P., Gualtieri, A., Marconcini, M., Tilton, J.C., Trianni, G., 2009. Recent advances in techniques for hyperspectral image processing. *Remote Sens. Environ.* 113 (Supplement 1), S110–S122.
- Pontius, R.G., Millones, M., 2011. Death to kappa: birth of quantity disagreement and allocation disagreement for accuracy assessment. *Int. J. Remote Sens.* 32 (15), 4407–4429.
- Procter, J., Cronin, S.J., Fuller, I.C., Lube, G., Manville, V., 2010. Quantifying the geomorphic impacts of a lake-breakout lahar, Mount Ruapehu, New Zealand. *Geology* 38 (1), 67–70.
- Procter, J.N., Cronin, S.J., Zernack, A.V., Lube, G., Stewart, R.B., Nemeth, K., Keys, H., 2014. Debris flow evolution and the activation of an explosive hydrothermal system; Te maari, tongariro, New Zealand. *J. Volcanol. Geotherm. Res.* 286, 303–316.
- Pullanagari, R.R., Keresztsuri, G., Yule, I.J., 2016. Mapping of macro and micro nutrients of mixed pastures using airborne AisaFENIX hyperspectral imagery. *ISPRS J. Photogramm. Remote Sens.* 117, 1–10.
- Pullanagari, R.R., Keresztsuri, G., Yule, I.J., 2017. Quantification of dead vegetation fraction in mixed pastures using AisaFENIX imaging spectroscopy data. *Int. J. Appl. Earth Obs. Geoinf.* 58, 26–35.
- Richter, R., Schlüpfer, D., 2002. Geo-atmospheric processing of airborne imaging spectrometry data. Part 2: Atmospheric/topographic correction. *Int. J. Remote Sens.* 23 (13), 2631–2649.
- Rogge, D., Rivard, B., Segl, K., Grant, B., Feng, J., 2014. Mapping of NiCu–PGE ore hosting ultramafic rocks using airborne and simulated EnMAP hyperspectral imagery, Nunavik, Canada. *Remote Sens. Environ.* 152 (0), 302–317.
- Salehi, S., Rogge, D., Rivard, B., Heincke, B.H., Fensholt, R., 2017. Modeling and assessment of wavelength displacements of characteristic absorption features of common rock forming minerals encrusted by lichens. *Remote Sens. Environ.* 199, 78–92.
- Scott, B.J., Potter, S.H., 2014. Aspects of historical eruptive activity and volcanic unrest at Mt. Tongariro, New Zealand: 1846–2013. *J. Volcanol. Geotherm. Res.* 286 (0), 263–276.
- Shane, P., Maas, R., Lindsay, J., 2017. History of Red Crater volcano, Tongariro Volcanic Centre (New Zealand): Abrupt shift in magmatism following recharge and contrasting evolution between neighboring volcanoes. *J. Volcanol. Geotherm. Res.*
- Spinetti, C., Carrère, V., Buongiorno, M.F., Sutton, A.J., Elias, T., 2008. Carbon dioxide of Pu'u'O'o volcanic plume at Kilauea retrieved by AVIRIS hyperspectral data. *Remote Sens. Environ.* 112 (6), 3192–3199.
- Spinetti, C., Mazzarini, F., Casacchia, R., Colini, L., Neri, M., Behncke, B., Salvatori, R., Buongiorno, M.F., Pareschi, M.T., 2009. Spectral properties of volcanic materials from hyperspectral field and satellite data compared with LiDAR data at Mt. Etna. *Int. J. Appl. Earth Observ. Geoinform.* 11 (2), 142–155.
- Stefano, P., Angelo, P., Simone, P., Filomena, R., Federico, S., Tiziana, S., Umberto, A., Vincenzo, C., Acito, N., Marco, D., Stefania, M., Giovanni, C., Raffaele, C., Roberto, D.B., Giovanni, L., Cristina, A., 2013. The PRISMA hyperspectral mission: science activities and opportunities for agriculture and land monitoring. 2013. IEEE International Geoscience and Remote Sensing Symposium - IGARSS. pp. 4558–4561.
- Sumner, J., Blake, S., Matela, R., Wolff, J., 2005. Spatter. *J. Volcanol. Geotherm. Res.* 142, 49–65.
- Sun, S., Hu, C., Feng, L., Swayze, G.A., Holmes, J., Graettinger, G., MacDonald, I., Garcia, O., Leifer, I., 2016. Oil slick morphology derived from AVIRIS measurements of the Deepwater Horizon oil spill: implications for spatial resolution requirements of remote sensors. *Mar. Pollut. Bull.* 103 (1–2), 276–285.
- Swayze, G.A., Clark, R.N., Goetz, A.F.H., Livo, K.E., Breit, G.N., Kruse, F.A., Sutley, S.J., Snee, L.W., Lowers, H.A., Post, J.L., Stoffregen, R.E., Ashley, R.P., 2014. Mapping advanced argillic alteration at Cuprite, Nevada, using imaging spectroscopy. *Econ. Geol.* 109 (5), 1179–1221.
- Tarquini, S., Favalli, M., Mazzarini, F., Isola, I., Fornaciai, A., 2012. Morphometric analysis of lava flow units: case study over LIDAR-derived topography at Mount Etna, Italy. *J. Volcanol. Geotherm. Res.* 235–236, 11–22.
- Tayebi, M.H., Tangestani, M.H., Vincent, R.K., Neal, D., 2014. Spectral properties and ASTER-based alteration mapping of Masahim volcano facies, SE Iran. *J. Volcanol. Geotherm. Res.* 287 (0), 40–50.
- Toniol, A.C., Galvão, L.S., Ponsoni, F.J., Sano, E.E., de Jesus Amore, D., 2017. Potential of hyperspectral metrics and classifiers for mapping Brazilian savannas in the rainy and dry seasons. *Remote Sens. Appl.: Soc. Environ.* 8, 20–29.
- Tortini, R., van Manen, S.M., Parkes, B.R.B., Carn, S.A., 2017. The impact of persistent volcanic degassing on vegetation: a case study at Turrialba volcano, Costa Rica. *Int. J. Appl. Earth Obs. Geoinf.* 59, 92–103.
- Townsend, D.B., Leonard, G.S., Conway, C.E., Eaves, S.R., Wilson, C.J.N., et al., 2017. Geology of the Tongariro National Park Area [Scale 1:60 000 Map], GNS Science Geological Map; 4. GNS Science, Lower Hutt, New Zealand: 1 Sheet + . 109 p. .
- Turner, R., Moore, S., Pardo, N., Keresztsuri, G., Uddstrom, M., Hurst, T., Cronin, S., 2014. The use of numerical weather prediction and a Lagrangian transport (NAME-III) and dispersion (ASHFALL) models to explain patterns of observed ash deposition and dispersion following the August 2012 Te Maari, New Zealand eruption. *J. Volcanol. Geotherm. Res.* 286 (0), 437–451.
- van der Meer, F., 2018. Near-infrared laboratory spectroscopy of mineral chemistry: a review. *Int. J. Appl. Earth Obs. Geoinf.* 65, 71–78.
- van der Meer, F.D., van der Werff, H.M.A., van Ruitenbeek, F.J.A., Hecker, C.A., Bakker, W.H., Noomen, M.F., van der Meijde, M., Carranza, E.J.M., Smeth, J.Bd., Woldai, T., 2012. Multi- and hyperspectral geologic remote sensing: a review. *Int. J. Appl. Earth Obs. Geoinf.* 14 (1), 112–128.
- van der Meer, F., Hecker, C., van Ruitenbeek, F., van der Werff, H., de Wijkerslooth, C., Wechsler, C., 2014. Geologic remote sensing for geothermal exploration: a review. *Int. J. Appl. Earth Obs. Geoinf.* 33, 255–269.
- van der Meer, F., Kopačková, V., Koucká, L., van der Werff, H.M.A., van Ruitenbeek, F.J.A., Bakker, W.H., 2018. Wavelength feature mapping as a proxy to mineral chemistry for investigating geologic systems: an example from the Rodalquilar epithermal system. *Int. J. Appl. Earth Obs. Geoinf.* 64, 237–248.
- Vane, G., Green, R.O., Chrien, T.G., Enmark, H.T., Hansen, E.G., Porter, W.M., 1993. The airborne visible/infrared imaging spectrometer (AVIRIS). *Remote Sens. Environ.* 44 (2–3), 127–143.
- Vaughan, R.G., Hook, S.J., Calvin, W.M., Taranik, J.V., 2005. Surface mineral mapping at Steamboat Springs, Nevada, USA, with multi-wavelength thermal infrared images. *Remote Sens. Environ.* 99 (1–2), 140–158.
- Villamor, P., Berryman, K.R., 2006. Late quaternary geometry and kinematics of faults at the southern termination of the Taupo Volcanic Zone, New Zealand. *N. Z. J. Geol. Geophys.* 49 (1), 1–21.
- Waske, B., Benediktsson, J.A., Árnason, K., Sveinsson, J.R., 2009. Mapping of hyperspectral AVIRIS data using machine-learning algorithms. *Can. J. Remote Sens.* 35 (sup1), S106–S116.
- Whelley, P.L., Glaze, L.S., Calder, E.S., Harding, D.J., 2014. LiDAR-derived surface roughness texture mapping: application to Mount St. Helens Pumice Plain Deposit Analysis. *IEEE Trans. Geosci. Remote Sens.* 52 (1), 426–438.
- Wilson, C.J.N., Houghton, B.F., McWilliams, M.O., Lamphere, M.A., Weaver, S.D., Briggs, R.M., 1995. volcanic and structural evolution of the Taupo Volcanic Zone, New Zealand: a review. *J. Volcanol. Geotherm. Res.* 68 (1–3), 1–28.
- Wyering, L.D., Villeneuve, M.C., Wallis, I.C., Siratovich, P.A., Kennedy, B.M., Gravley, D.M., Cant, J.L., 2014. Mechanical and physical properties of hydrothermally altered rocks, taupo volcanic zone, New Zealand. *J. Volcanol. Geotherm. Res.* 288, 76–93.
- Yule, I.J., Pullanagari, R.R., Keresztsuri, G., 2016. Detecting subtle environmental change: a multi-temporal airborne imaging spectroscopy approach. SPIE 2016 Proceedings, Remote Sensing for Agriculture, Ecosystems, and Hydrology XVIII 9998, 1–7.